Journal of Materials Chemistry A

ROYAL SOCIETY OF CHEMISTRY

PAPER

View Article Online
View Journal | View Issue

Cite this: J. Mater. Chem. A, 2023, 11, 9160

Predicting the Na^+ ion transport properties of NaSICON materials using density functional theory and Kinetic Monte Carlo†

Judith Schuett,[ab] Antonia S. Kuhn[b] and Steffen Neitzel-Grieshammer *[b]

The efficiency of all-solid-state Na^+ ion batteries crucially depends on the applied electrolyte, among which sodium super ionic conductors (NaSICONs) show high ionic conductivities. However, the experimental data on ionic conductivities available in the literature vary by several orders of magnitude depending on composition and sample preparation. Hence, a comprehensive understanding of Na^+ transport properties is still lacking. In this study, we investigate the multi-cationic NaSICONs $Na_{1+x}M_2Si_xP_{3-x}O_{12}$ (with M = Zr^{4+}, Hf^{4+}, Sn^{4+}, and $0 \leq x \leq 3$) by combining state-of-the-art computational tools, namely density functional theory calculations to analyse the structure at the atomic level and Kinetic Monte Carlo simulations to study the ion transport on the macroscopic level. The results show that there is no simple correlation between structural properties and the Na^+ ion transport as often described in the literature. Rather the interplay of the ratio of unoccupied to occupied charge carrier sites, interactions between Na^+ ions and adjacent cations, and Na^+ migration barriers, which are influenced by both the M-cation and the degree of substitution, must be considered. Our study provides a detailed picture of the complex ion transport in NaSICONs of variable composition.

Received 25th January 2023
Accepted 27th March 2023

DOI: 10.1039/d3ta00440f

rsc.li/materials-a

1 Introduction

Although Na^+ ion conducting NaSICON materials were discovered more than 50 years ago[1–3] and have been intensively studied in recent years,[4–12] the examined compositional range of NaSICONs is still limited, and a thorough understanding of Na^+ ion transport seems to be lacking.

NaSICONs are attractive candidates among solid-state electrolytes (SSEs) because they exhibit good thermal and (electro) chemical stability, high three-dimensional ionic conductivity at room temperature,[13–19] and demonstrate promising performance for all-solid-state sodium-ion batteries (NIBs).[20–33] NIBs are considered a complementary system to the market-leading lithium-ion batteries, especially for large-scale energy storage, due to the similar chemical properties of sodium and lithium, the long-term resource availability of sodium, and the cost reduction of NIBs.[34–48] In addition, all-solid-state NIBs using SSEs are characterized by a long device lifetime, potentially high safety, wide operating temperature range, and high energy and power density depending on the cell architecture.[13,17–19,49–52]

Various review articles summarize the developments and challenges of NaSICON materials for all-solid-state NIBs.[4–12] NaSICON structures with the general formula $Na_xM_2(AO_4)_3$, exhibit a flexible framework in which various M and A cations can be incorporated. Therefore, they offer a large compositional diversity allowing a wide range of applications, but also leading to ionic conductivities that vary over orders of magnitude. Ma *et al.* reported one of the highest total conductivities among NaSICONs to date of 5.2×10^{-3} S cm^{-1} at 25 °C for $Na_{3.4}Zr_2Si_{2.4}P_{0.6}O_{12}$, which is comparable with state-of-the-art liquid-based electrolytes for NIBs and highlights the promising potential of NaSICONs as SSEs.[26]

Substitution of both M and A cations has been shown to be an effective strategy for modifying the (electro)chemical and structural properties, and thus the ionic conductivity of NaSICONs. However, the ionic conductivity of NaSICONs depends not only on the composition but also on the sample preparation and the measurement techniques.[9,18,53,54] Due to the large scatter of experimental data currently available, a thorough understanding of Na^+ transport properties based on these data is difficult.[18] Computational methodologies can be utilized to elucidate the microscopic properties, such as the structure and the migration energy profile of ionic pathways, and their influences on the macroscopic transport behaviour.[54–59] To date, however, the focus of computational studies has been mainly on the parent composition $Na_{1+x}Zr_2Si_xP_{3-x}O_{12}$,[1–3] which is not sufficient for an adequate understanding of NaSICONs.[53,60–69] Therefore, there is a need to investigate various substituted

[a]Helmholtz-Institut Münster (IEK-12), Forschungszentrum Jülich GmbH, Corrensstraße 46, 48149 Münster, Germany

[b]Institute of Physical Chemistry, RWTH Aachen University, Landoltweg 2, 52056 Aachen, Germany. E-mail: steffen.grieshammer@rwth-aachen.de

† Electronic supplementary information (ESI) available. See DOI: https://doi.org/10.1039/d3ta00440f

structures over entire compositional ranges using reliable, low-effort computational techniques. Thus, a more comprehensive understanding of the influences of microscopic Na^+ ion motion on macroscopic transport properties can be obtained, guiding the material design of NaSICON solid-state electrolytes.

In our previous study, we proposed a first-principles based Kinetic Monte Carlo (KMC) model considering the local ionic environment and the migration energies of the charge carriers which is highly suitable to describe Na^+ ion transport in the NaSCION structure.[70] On the one hand, the model is based on Density Functional Theory (DFT) calculations, ensuring a reliable description of the structure at the microscopic level. On the other hand, the KMC simulations allow the investigation of transport properties both on long timescales and in large crystalline systems capturing a great number of ion transport events and accounting for statistical variances. However, the approach comes along with a high amount of DFT calculations and is thus not applicable to a broad range of elements.[70] Nevertheless, the suitability of this approach was recently confirmed by the study of Deng *et al.* using a combination of local-cluster expansion, DFT-NEB migration barriers, and KMC.[53]

In the present study, we show an improved approach based on our previously proposed KMC model that requires DFT calculations with minimized computational effort, yet provides higher accuracy by considering a wider range of the local ionic environment. Hence, this approach is suitable for the study of the influence of various substituents and temperatures on the ionic diffusion of multi-element NaSICONs of arbitrary compositions.

We demonstrate the suitability of the approach by studying $Na_{1+x}M_2Si_xP_{3-x}O_{12}$ (with M = Zr^{4+}, Hf^{4+}, Sn^{4+} and $0 \leq x \leq 3$) as example compositions for multi-element NaSICON-type conductors. These M-cations were selected to investigate structures that exhibit rhombohedral symmetry over a wide temperature range and show the same migration mechanism for Na^+ ions. Not only the influence of Si^{4+} substitution on P^{5+} sites, but also the influence of chemical and structural factors of homovalent M^{4+} substitution on Na^+ ion transport is investigated.

2 Structure and ionic migration

The original NaSICON material with composition $Na_{1+x}Zr_2Si_xP_{3-x}O_{12}$ exhibits rhombohedral structure ($R\bar{3}c$) (see Fig. 1) but shows a monoclinic ($C2/c$) distortion for $1.6 \leq x \leq 2.4$ at room temperature.[2,3,53,71–76] However, at temperatures above 150 °C only the rhombohedral phase exists.[53,72,77,78]

In this study, we focus on the rhombohedral structure. On the one hand, this phase exists over a larger compositional and temperature range. On the other hand, we have shown in our previous study that bond distances, ionic interaction energies, and migration energies are very similar in the monoclinic and rhombohedral structures. Therefore, the following analysis and conclusions can be adopted for the monoclinic structure.[70]

As shown in Fig. 1, the rhombohedral structure consists of a rigid three-dimensional framework of corner-sharing MO_6 octahedra and PO_4 tetrahedra.[1–3,61,62,74,75,79,80] Two distinct sodium

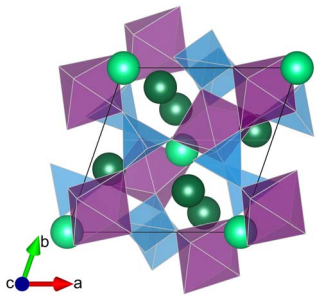

Fig. 1 The primitive rhombohedral NaSICON structure $Na_{1+x}M_2Si_xP_{3-x}O_{12}$. Key: Na1 (light green), Na2 (dark green), MO_6 (purple), PO_4/SiO_4 (blue).

ion sites, the Na1 (6b) and Na2 (18e) sites, are located in the scaffold cavities. The Na1 site is energetically more favourable and the sublattice is fully occupied at all substitution degrees x.[1–3,53,62,64,67,68,73–76,79–82] As x increases, Si^{4+} substitute P^{5+} ions and the amount of Na^+ ions on Na2 sites increases to maintain the overall charge neutrality.[2,3] Transient metastable mid-Na sites located between Na1 and Na2 sites have been reported.[61,66,75,76,83] However, the occupation of the mid-Na sites is negligible and tends to zero at high Na^+ concentrations, since the occupation of the Na1 and Na2 sites excludes the occupation of the mid-Na sites due to the small distance.[61,66,68,76] Therefore, we focus on the equilibrium sodium sites, Na1 and Na2, in this work.

The NaSICON structure, which has a large number of Na^+ ion sites and thus a high charge carrier concentration, exhibits fast, three-dimensional Na^+ ion diffusion within the rigid framework.[2,3,66] As illustrated in Fig. 2, Na2 ions move towards occupied Na1 sites and push the Na1 ions onto adjacent unoccupied Na2 sites.[2,3,53,61,63,64,66,68,74,84–86] This correlated pushing-out mechanism is based on Coulomb repulsion and the potential energy transfer from ions at energetically higher Na2 sites to ions at lower Na1 sites.[3,53,58,66,68,87,88] Bottlenecks of the migration pathway are formed by PO_4- and ZrO_6-polyhedra edges, depicted as red triangles.[2,3,69,84,85,89,90] At high substitution concentration, a local minimum occurs along the migration path corresponding to the transient mid-Na site allowing fast Na^+ ion diffusion.[61,66,68,75,76,83] Three different migration pathways of 80°,

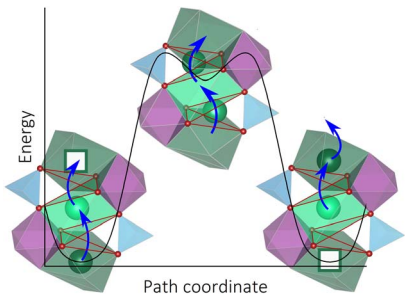

Fig. 2 Correlated pushing-out mechanism shown with blue arrows. One Na2 ion moves towards a Na1 ion pushing it onto an adjacent unoccupied Na2 site. The bottlenecks depicted as red triangles are formed by PO_4- and ZrO_6-polyhedra edges. The occupation of the opposing mid-Na sites by the migrating Na^+ ions corresponds to a local minimum at high substitution concentration. Key: Na1 (light green), Na2 (dark green), MO_6 (purple), PO_4/SiO_4 (blue), O (red).

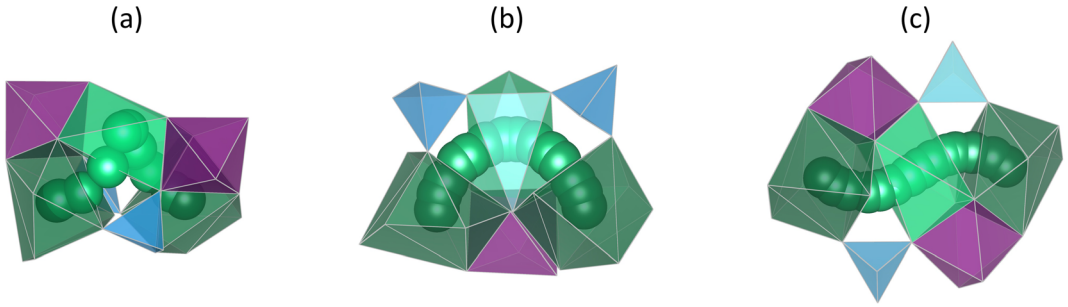

Fig. 3 The different Na^+ migration pathways according to the angle between the Na2–Na1–Na2 sites involved in the migration of (a) 80°, (b) 90°, and (c) 180°. Key: Na1 (light green), Na2 (dark green), MO_6 (purple), PO_4/SiO_4 (blue).

90° and 180° are distinguished according to the angle between the Na2–Na1–Na2 sites involved in the migration, as depicted in Fig. 3.[68,70] We have previously shown that the high conductivity and low activation energy of compositions with $1.8 \leq x \leq 2.5$ [3,72] is not only attributed to (i) favourable ratio of charge carrier and vacancy concentration,[6,26,53,66,69,76,81,87,91,92] (ii) high Na^+–Na^+ coulombic repulsion which enhances the correlated migration,[2,58,66,68,69,76,83,87] and (iii) widening of the bottleneck[6,68,69,73,74,84,85,89,90] as described in the literature, but also to (iv) percolation of sodium ions in favourable silicon rich environments.[53,70]

3 Methods

3.1 Density functional theory calculations

3.1.1 General computational setup. All calculations were performed by Kohn–Sham DFT[93,94] with the Vienna *Ab Initio* Simulation Package (VASP).[95–98] The Generalized Gradient Approximation (GGA) functional parametrized by Perdew–Burke–Ernzerhof (PBEsol) was implemented.[99] The projector augmented wave (PAW) method was applied.[100] The electronic and ionic relaxation convergence criteria were set to 10^{-4} eV and 0.01 eV $Å^{-1}$, respectively. A *k*-point mesh centred at the gamma point according to the Monkhorst–Pack scheme was used to sample the Brillouin zone.[101] The $2p^6 3s^1$ electrons of sodium, the $3s^2 3p^3$ electrons of phosphorus, the $3s^2 3p^2$ electrons of silicon, the $2s^2 2p^4$ electrons of oxygen, the $5s^2 4d^{10} 5p^2$ electron of tin, the $5p^6 6s^2 5d^2$ electrons of hafnium and the $4s^2 4p^6 4d^2 5s^2$ electron of zirconium were considered as valence electrons.

3.1.2 Cell transformation. First, the relaxation of the rhombohedral primitive cell of $Na_1M_2P_3O_{12}$ ($M = Zr^{4+}$, Hf^{4+}, Sn^{4+}) with 36 atoms was performed with a $2 \times 2 \times 2$ *k*-point mesh and plane waves with an energy cut-off of 520 eV. The volume, ion positions and stress tensors were relaxed simultaneously. The optimized primitive cell was then transformed into a cubic cell with 144 atoms according to the rotation matrix:

$$P = \begin{pmatrix} 1 & 1 & -1 \\ -1 & 1 & 1 \\ 1 & -1 & 1 \end{pmatrix}$$

The Na1 sublattice was fully occupied in all cells while the Na2 sublattice was empty. As described below, the optimisation of the ion positions was performed using $1 \times 1 \times 1$ *k*-point mesh and plane waves with an energy cut-off of 400 eV.

3.1.3 Site energies. The influence of the local environment on the Na^+ site energies was investigated for the composition $Na_1M_2P_3O_{12}$ ($M = Zr^{4+}$, Hf^{4+}, Sn^{4+}). The cubic cell was enlarged to 576 atoms to mitigate finite size effects. Two Na^+ ions were introduced on Na2 sites to investigate Na^+–Na^+ interactions. A homogenous background charge was taken into account compensating the introduced defect charge of +2. To investigate the Na^+–Si^{4+} interactions, one P^{5+} ion was substituted by a Si^{4+} ion and one Na^+ ion was introduced on the Na2 site to maintain the charge neutrality.

3.1.4 Coulomb energies. The introduction of a Si^{4+} ion on a P^{5+} site creates a −1 charged defect, while the introduction of a Na^+ ion on a vacant Na2 site corresponds to a +1 charged defect.

The Coulomb energies between the introduced defects at a distance d were calculated according to eqn (1) using the relative permittivity ε_r and the Born effective charges q_B determined in the primitive cells $Na_1M_2P_3O_{12}$ ($M = Zr^{4+}$, Hf^{4+}, Sn^{4+}) with 37 atoms by Density Functional Perturbation Theory (DFPT) (Tables S4 and S5†).[102–104]

$$E = \frac{q_1 q_2}{4\pi\varepsilon d} \quad (1)$$

The permittivity is defined as $\varepsilon = \varepsilon_r \varepsilon_0$ with the permittivity of the vacuum ε_0. The defect charges are defined as $q = q_{B,rel} e$ with the Born effective charge of the substituted lattice site $q_{B,rel}$ calculated according to eqn (2).

$$q_{B,rel} = q_{B,sub} - q_{B,org} \quad (2)$$

Here, $q_{B,org}$ and $q_{B,sub}$ is the Born effective charge of the original ion and the substituent, respectively.

3.1.5 Migration energies. The correlated migration of two sodium ions was calculated in the cubic cell for $Na_{1+x}M_2Si_xP_{3-x}O_{12}$ ($M = Zr^{4+}$, Hf^{4+}, Sn^{4+}) with $x = 0$ and $x = 3$. In the case of the unsubstituted structure ($x = 0$), one additional Na^+ ion was introduced on the Na2 site resulting in cells with 145 atoms. In the case of the fully substituted structure ($x = 3$), one vacancy was created by removing one Na^+ ion from a Na2 site resulting in a cell

with 167 atoms. The defect charges were compensated by a uniform background charge. The minimum energy migration paths in 80°, 90° and 180° were determined by the Climbing Image Nudged Elastic Band (CI-NEB) method with five interpolated images.[105–107]

3.2 Kinetic Monte Carlo

The KMC method was used to simulate the macroscopic sodium ion long-range transport in the NaSICONs by evaluating large stochastic ensembles of sodium ion jumps.[55,57,108,110] According to transition state theory, the ionic jump is defined by the energy wells of its stable initial and final state, which are separated by an energy barrier E_{mig}. E_{mig} is the difference between the saddle point and the ground state of the energy surface along the migration path and corresponds to the unstable intermediate transition state.[57,110,111] The Boltzmann distribution gives the probability P for the success of the jump, *i.e.*, for the Na^+ ions to overcome E_{mig} when possessing sufficiently large kinetic energy.

$$P = \exp\left(-\frac{E_{mig}}{k_B T}\right) \tag{3}$$

Here, k_B is the Boltzmann constant and T the temperature.

The frequency Γ of the sodium ion jump is given by eqn (4).[57,110,111]

$$\Gamma = \nu \cdot \exp\left(-\frac{E_{mig}}{k_B T}\right) \tag{4}$$

In this study, the attempt frequency associated with the ion vibration is assumed to be $\nu = 10^{13}$ Hz.[110]

The mobility of Na^+ ions μ_{Na} resulting from successful jumps is evoked when an external electric field $\vec{E}$ is applied and the Na^+ ions move parallel to the direction of $\vec{E}$. μ_{Na} is given by the drift velocity $\vec{u}_{Na}$, *i.e.*, the average ionic displacement $\Delta\vec{x}_{Na}$ per unit time t, in the applied electric field $\vec{E}$.

$$\mu_{Na} = \frac{|\vec{u}_{Na} \cdot \vec{E}|}{|\vec{E}|^2} = \frac{|\Delta\vec{x}_{Na} \cdot \vec{E}|}{|\vec{E}|^2 \cdot t} \tag{5}$$

The simulated time t is defined by the number of charge carriers N_{Na}, their number of jump attempts $N_{attempt}$ as well as averaged number of jump possibilities N_{Jump}, and the attempt frequency ν.

$$t = \frac{N_{attempt}}{N_{Na} \cdot \langle N_{Jump} \rangle \cdot \nu} \tag{6}$$

The ionic conductivity σ_{Na} results from the Na^+ ion concentration c_{Na} and mobility μ_{Na}, and the charge q_{Na}.

$$\sigma_{Na} = c_{Na} \cdot \mu_{Na} \cdot |q_{Na}| \tag{7}$$

According to Ohm's law, the drift velocity $\vec{u}_{Na}$ and thus the current density $\vec{j}_{Na}$, is proportional to $\vec{E}$ with μ_{Na} or σ_{Na}, respectively, being the constant of proportionality.

$$\vec{u}_{Na} = \mu_{Na} \cdot \vec{E} \tag{8}$$

with

$$\vec{u}_{Na} = \frac{\vec{j}_{Na}}{|q_{Na}| \cdot n_{Na}} \tag{9}$$

$$\vec{j}_{Na} = \sigma_{Na} \cdot \vec{E} \tag{10}$$

Thus, the Na^+ ion conductivity must be independent of the constant external field which is ensured at the field strength of $\vec{E} = 107$ V m^{-1} applied in the KMC simulations (Fig. S1†).[70]

KMC simulations were performed in 10 × 10 × 10 cells of $Na_{1+x}M_2Si_xP_{3-x}O_{12}$ ($M = Zr^{4+}$, Hf^{4+}, Sn^{4+}) for the compositional range of $0.2 \leq x \leq 2.8$ and temperature range of 450 K $\leq T \leq$ 700 K using the program MOCASSIN with the null-event algorithm.[109]

4 KMC model

As shown in eqn (3), the migration barrier must be known for KMC simulations. However, different local environments of the migrating Na^+ ions lead to different energies of the initial and final states making the energy barrier E_{mig} dependent on the jump directions. Thus, E_{mig} of each jump is defined by the energy of the end states E_{conf} and the directional independent migration energy $E_{mig,0}$.[57,110,112]

$$E_{mig} = \frac{E_{conf,f} - E_{conf,i}}{2} + E_{mig,0} \tag{11}$$

In our previous study, we investigated the configurational energy E_{conf} and migration energy $E_{mig,0}$ for $Na_{1+x}Zr_2Si_xP_{3-x}O_{12}$ ($x = 0, 1, 2, 3$) using DFT.[70] The calculation of the exact energy of all possible configurations exceeds the computational limit. However, we have shown that they can be predicted with sufficient accuracy based on the DFT calculations of a few compositions using the models described below.[70]

4.1 Configurational energy

The configurational energy E_{conf} describes the energy of the cell resulting from the sum of sodium site energies. The sodium site energies depend on the local cationic environment and thus on the distribution of Si^{4+}/P^{5+} ions and the occupation of Na2 sites. E_{conf} is described by a pair interaction model according to eqn (12).[70]

$$E_{conf} = \sum_{i=2} {N_{Na}}^i \cdot {E_{Na}}^i + \sum_{i=1} {N_{Si}}^i \cdot {E_{Si}}^i \tag{12}$$

Here, N^i_{Na} and N^i_{Si} is the number of Na^+–Na^+ pairs and Na^+–Si^{4+} pairs in iNN distance, respectively, with the corresponding interaction energies E_{Na} and E_{Si}. The Na1 sites located in 1NN distance are omitted as we assume them to be fully occupied as described in literature.[1–3,53,62,64,67,68,73–76,79–82]

4.2 Migration energy

The migration energy $E_{mig,0}$ depends on the migration pathway and the substitution degree. $E_{mig,0}$ of the migration in 80°, 90° and 180° of all substitution fractions can be described by the interpolation between the migration energies in the non-substituted cell with $x = 0$ and the fully substituted cell with $x = 3$ according to eqn (13).[70]

$$E_{mig,0}(x) = \frac{x\left(E_{mig,0}(x=3) - E_{mig,0}(x=0)\right)}{3} + E_{mig,0}(x=0) \quad (13)$$

5 Investigation at the atomistic level

5.1 Configurational energies

The configurational energies are described by the simple pair interaction model according to eqn (12). We have shown in our previous study that the pair interaction energies can be determined by fitting many different configurations of $Na_{1+x}M_2Si_xP_{3-x}O_{12}$ with $0 \leq x \leq 3$.[70] However, this approach requires a large computational effort and is therefore not feasible for the exploration of compositions with various M-cationic species. In contrast, in this study we calculate the Na^+–Na^+ and Na^+–Si^{4+} pair interaction energies depending on the Na^+–cation distances in larger cells with minimal substitution concentration. In this way, the pair interactions can be investigated individually without considering additional compositional effects. This approach allows the study of Na^+–cation interactions with a greater range while requiring less computational effort. Here, the Na^+–Na^+ and Na^+–Si^{4+} pair interactions are investigated for the composition $Na_1M_2P_3O_{12}$ (M = Zr^{4+}, Hf^{4+}, Sn^{4+}). For this purpose, a pair of a Na^+ ion and another cation (Na^+ or Si^{4+}) are introduced into the unsubstituted cell. The pair interaction energy is calculated relative to the cell with the furthest Na^+–cation distance.

Finite size effects are assumed to be negligible when describing the pair interaction energies. Even in the case of the cell with the farthest distance between the introduced cations, the distance to these cations in the neighbouring imaged cells is nevertheless much larger ($d_{Na^+\text{–cation}} > 19$ Å).

5.1.1 Na^+–Na^+ pair interaction. Fig. 4 shows the interaction energies (red circles, blue traingles, green squares) and Coulomb energies (pink lines) as a function of the Na2–Na2 distance in $Na_1M_2P_3O_{12}$ (M = Zr^{4+}, Hf^{4+}, Sn^{4+}). For all compositions, the Na2–Na2 repulsion decreases with distance and is negligible for distances greater than 9.9 Å.

The Na2–Na2 interaction energies are in good agreement with the Coulomb energies indicating that electrostatic effects are dominant. However, the cation arrangement also affects the interaction energies when the Na2 ions are in the same coordination environment, *i.e.*, at small Na2–Na2 distances, leading

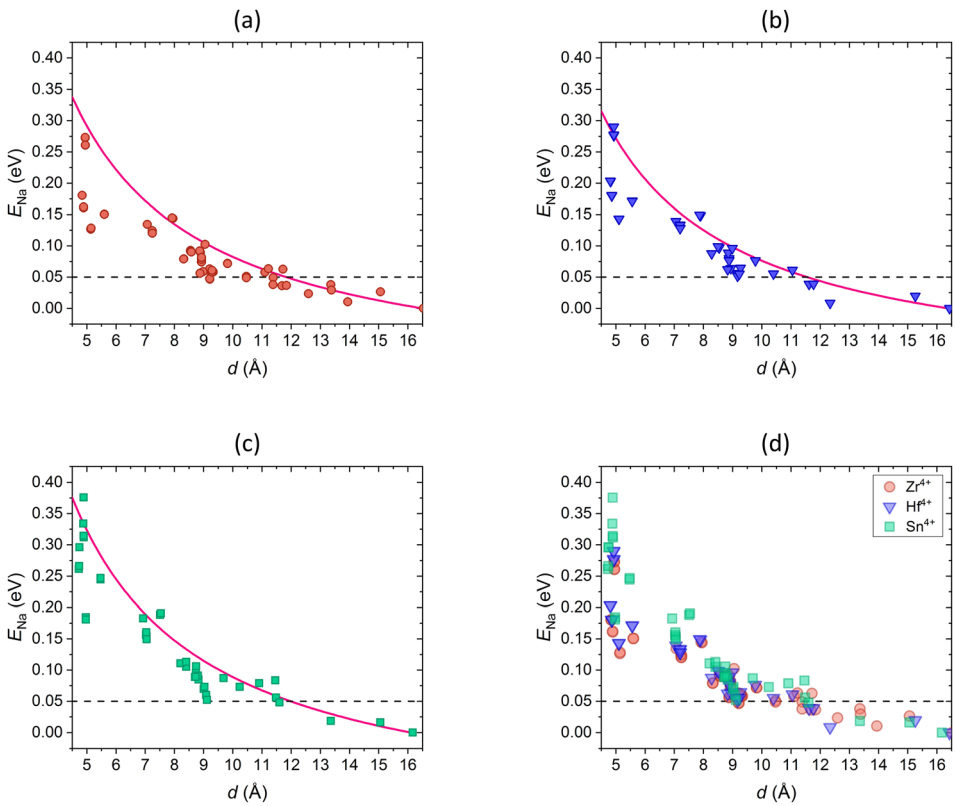

Fig. 4 Na^+–Na^+ Coulomb energies (pink line) and interaction energies E_{Na} of the structure $Na_1M_2P_3O_{12}$ with (a) M = Zr^{4+} (red), (b) M = Hf^{4+} (blue), (c) M = Sn^{4+} (green), and (d) comparison of E_{Na} of all compositions dependent on Na2–Na2 distances *d*. The dotted line shows the energy limit of E_{Na} = 0.05 eV below which pair interactions are neglected.

to the largest deviations between the Na2–Na2 interaction energies and the Coulomb energies.

The compositions $Na_1M_2P_3O_{12}$ with M = Zr^{4+} (Fig. 4a) and M = Hf^{4+} (Fig. 4b) exhibit similar pair interaction energies due to the similar ionic radii of $r^{4+}_{Zr} = 0.72$ Å and $r^{4+}_{Hf} = 0.71$ Å[113] and thus similar cell volumes (Fig. S2†) and bond distances (Table S1†).

In the composition with M = Sn^{4+} (Fig. 4c) the interaction energies of Na2–Na2 ions at smaller distances are larger than in the compositions with M = Zr^{4+}, Hf^{4+} but align at larger distances. The volume of the cell with M = Sn^{4+} is smaller than that of the cells with M = Zr^{4+}, Hf^{4+} due to the smaller ionic radii of $r^{4+}_{Sn} = 0.69$ Å (Fig. S2†).[113] Therefore, the bond distances in the structure with M = Sn^{4+} are smaller (Table S2†) which has a stronger effect on the interactions energies the smaller the distances of Na2–Na2 pairs are.

5.1.2 Na^+–Si^{4+} pair interaction. Fig. 5 shows the relative energies (red circles, blue traingles, green squares) and the Coulomb energies (pink lines) in dependence on the Na2–Si distance of all compositions (M = Zr^{4+}, Hf^{4+}, Sn^{4+}). As expected, the attractive Na2–Si pair interactions weaken with increasing distances and are negligible for distances beyond 8.7 Å.

The calculated interaction energies cannot be described sufficiently by the Coulomb energies. Since the SiO_4 tetrahedra are part of the structural framework, Si^{4+} may not be considered a point defect due to its high covalent bonding character. Thus, the pair interaction energies may depend not only on electrostatic effects but also on elastic effects describing deformation or distortions of the lattice, as also observed in doped zirconia[114] and ceria.[115,116] The elastic effects are expected to be stronger when the Na2–Si distance is small and the coordination environments of the introduced Na^+ and Si^{4+} ion affect each other. With increasing distances, the elastic effects may be less pronounced and differences between interaction and coulombic energies are smaller.

The Na2–Si interaction energies in the compounds with M = Zr^{4+} (Fig. 5a) and M = Hf^{4+} (Fig. 5b) agree due to similar structural properties as discussed above. Moreover, Zr^{4+} and Hf^{4+} are both transition elements and exhibit the same valence electron configuration of d^0.

In comparison, the composition with M = Sn^{4+} (Fig. 5c) exhibits stronger Na2–Si interactions at a small distance. On the one hand, this can be attributed to the smaller cell volume and thus smaller bond distances as described above. On the other hand, Sn^{4+} is a main-group element with a different valence electron configuration of d^{10}, which may have an additional impact. Rodrigo *et al.* stated that unoccupied orbitals as in the compositions with M = Zr^{4+}, Hf^{4+} exhibiting d^0 valence electron configuration allow greater structural flexibility. In contrast, fully occupied d-orbitals as in the compositions with M = Sn^{4+} lead to more rigid bonds.[117] Thus, cells containing d^0 M-cations may accommodate substituents with lower energy cost

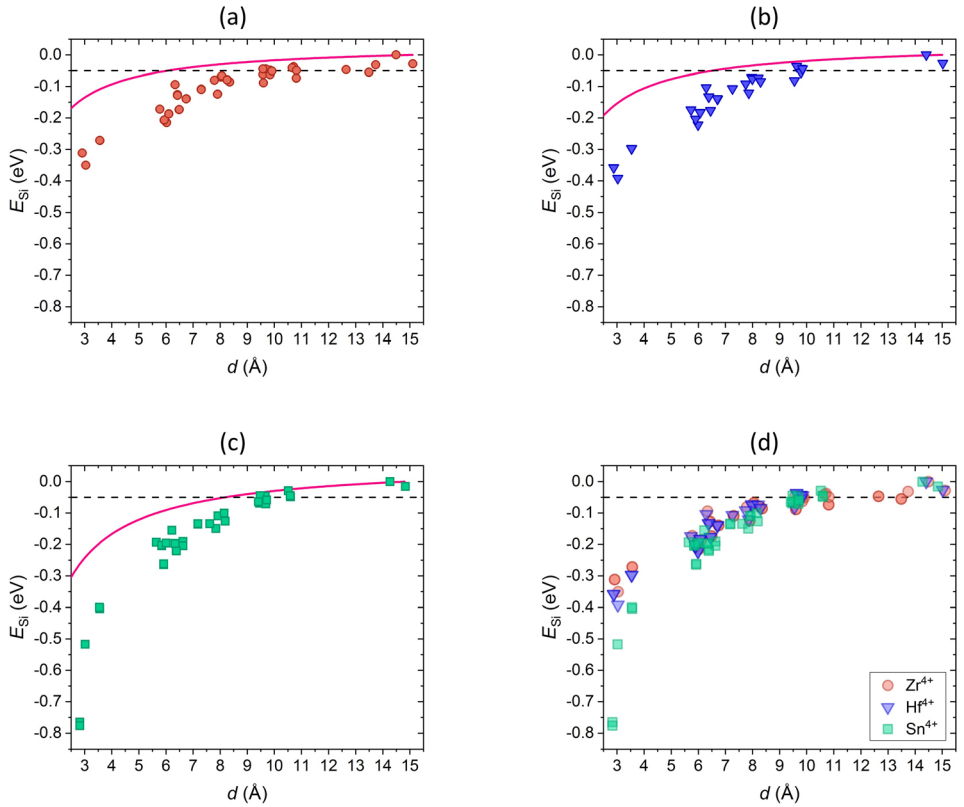

Fig. 5 Na^+–Si^{4+} Coulomb energies (pink) and interaction energies E_{Si} of the structure $Na_1M_2P_3O_{12}$ with (a) M = Zr^{4+} (red), (b) M = Hf^{4+} (blue), (c) M = Sn^{4+} (green), and (d) comparison of E_{Si} of all compositions dependent on Na2–Si distances *d*. The dotted line shows the energy limit of $E_{Si} = -0.05$ eV below which pair interactions are considered.

compared to cells with d^{10} M-cations. Influences of the different electronic structure of the M-cations on structure and crystal symmetry among $Na_xM^{4+}_{2-x}M^{3+}_x(PO_4)_3$ have also been observed in other studies.[117–122]

In summary, the comparison of NaSCION structures with different M-cations shows that the compounds with M = Zr^{4+}, Hf^{4+} are not only isovalent but also isostructural, whereas this is not true for the structure with M = Sn^{4+}, which is in agreement with previous studies.[117,120,122,123]

In our previous approach to determine configurational energies, only Na2–Na2 pairs in a distance up to 5.1 Å and Na2–Si pairs up to 3.7 Å were considered due to the small size of the cell with 168 atoms. We described the pair interaction energies only dependent on the distance by grouping cations according to similar distance from the Na2 ions. The pair interaction energies of $Na_{1+x}Zr_2Si_xP_{3-x}O_{12}$ ($0 \le x \le 3$) were fitted according to eqn (12) taking into account 754 configurations whose energies were calculated using DFT.[70] However, in this study, we show that Na2–Na2 pairs in distances up to 9.9 Å and Na2–Si pairs in distance up to 8.7 Å affect the configurational energy of the cell. The pair interaction energies depend not only on electrostatic effects but also on the cationic coordination and elastic effects at small Na-cation distances and must be considered to describe the configurational energy accurately. We show that calculating only 50 structures with the least substitution and varying Na2-cation distances is sufficient to individually determine all pair interaction energies that affect the overall configurational energy, and thus be able to predict E_{conf}. Additionally, structures with composition $Na_4M_2Si_3O_{12}$ (M = Zr^{4+}, Hf^{4+}, Sn^{4+}) in which one P^{5+} ion was introduced onto a Si^{4+} site creating one vacancy on Na2 site (V_{Na}) were investigated. By varying the distance between the P^{5+} and the V_{Na}, the Na^+–Si^{4+} interaction in highly substituted systems can be deduced as the number of corresponding pairs changes. The results show the expected trend for all compositions: The cells in which P^{5+} is in the nearest neighbour position to V_{Na} are energetically more favourable than the cells in which P^{5+} and V_{Na} are far apart, implying that the configurational energy is lowered by Si^{4+} near the Na2 positions (Table S3†).

Overall, despite the computation of larger cells of 578 atoms, this approach can significantly reduce the computational effort and therefore allows the study of NASICON materials with a wide range of compositions.

5.2 Migration energies

The different migration pathways of about 80°, 90° and 180° were calculated for the unsubstituted ($x = 0$) and the fully substituted ($x = 3$) system $Na_{1+x}M_2Si_xP_{3-x}O_{12}$ (M = Hf^{4+}, Sn^{4+}). The results for Zr^{4+} are taken from our previous study.[70] The energy profiles of the different migration paths in all compositions are shown and discussed in more detail in Section 4 in the ESI.† The migration energies $E_{mig,0}$ of $x = 0$ and $x = 3$ were calculated according to eqn (11) and then predicted for arbitrary substitution concentrations x by linear interpolation according to eqn (13), as shown in Fig. 6.

5.2.1 Dependence on migration path. In all compositions $E_{mig,0}$ decreases with increasing angle of migration pathway due to less steric hindrance of the migrating Na^+ ions. Moreover, the decrease of the migration energy with x is the most for the 80° migration and the least for the 180° migration. Hence, the differences in $E_{mig,0}$ for different angles are largest for $x = 0$ and decrease with increasing x. As the substitution level increases, the influence of the ions adjacent to the migration path becomes greater, as explained below.

5.2.2 Dependence on substitution degree. With increasing x, P^{5+} is replaced by larger Si^{4+} and the amount of Na^+ increases. This leads to three main factors affecting the migration energy, which have been emphasized in previous studies on Na^+ mobility and conductivity in NaSICONs: (i) increasing attractive interactions of the migrating Na^+ ions and surrounding Si^{4+} ions,[53,63,64] (ii) increasing repulsive interactions of the migrating Na^+ ions and surrounding Na^+ ions,[2,66,68,69,76,83] (iii) increasing size of the bottleneck.[6,68,69,73,74,84,85,89,90,124] In the following, these factors are examined in more detail to evaluate their impact on the migration energy.

(i) The amount of Si^{4+} near the migration pathway in the structure $Na_1Zr_2P_3O_{12}$ ($x = 0$) was gradually increased to determine the influence of the interactions between the migrating Na^+ and surrounding Si^{4+} on the migration energy. The Si^{4+} sites to be occupied are illustrated in Fig. S5.† Fig. 7 shows the resulting migration energies dependent on the number of Si^{4+} near the migration pathway. With increasing Si^{4+}

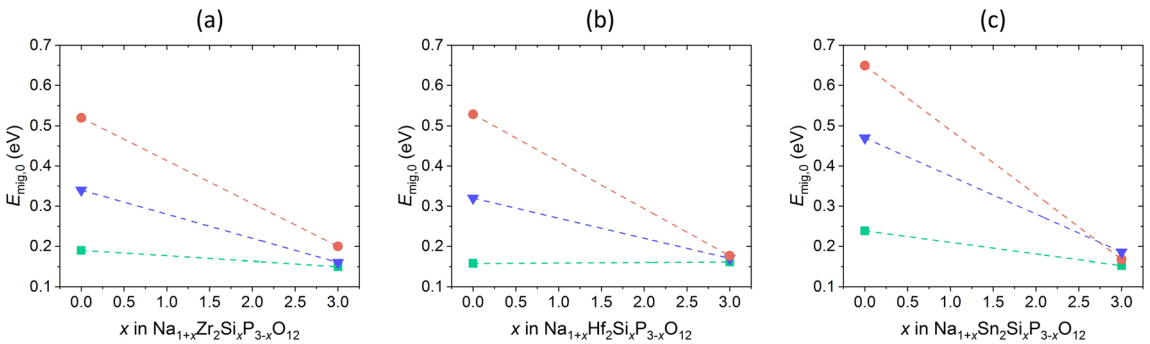

Fig. 6 Interpolated migration energies $E_{mig,0}$ dependent on the subsitution degree x of $Na_{1+x}M_2Si_xP_{3-x}O_{12}$ with (a) M = Zr^{4+} (taken from ref. 70), (b) M = Hf^{4+}, (c) M = Sn^{4+} of the pathway in 80° (red), 90° (blue) and 180° (green) according to eqn (13).

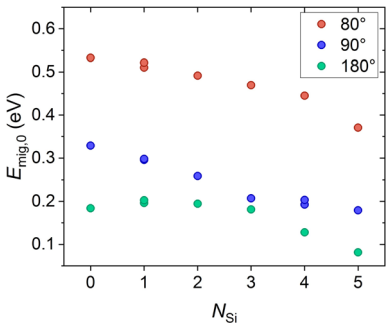

Fig. 7 Migration energy $E_{mig,0}$ of the pathways in 80° (red), 90° (blue) and 180° (green) dependent on the amount of Si^{4+} $N_{Si^{4+}}$ adjacent to the migration pathway in the structure with composition $Na_1Zr_2P_3O_{12}$.

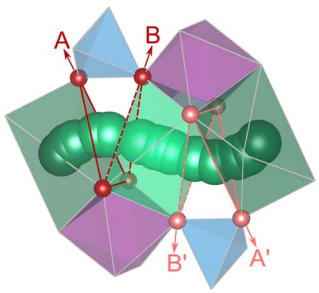

Fig. 9 Bottlenecks of the 180° migration path in $Na_{1+x}M_2Si_xP_{3-x}O_{12}$ formed by three O^{2-} ions of SiO_4/PO_4 tetrahedra and MO_6 octahedra. Key: Key: Na1 (light green), Na2 (dark green), O (red), SiO_4/PO_4 (blue), M/MO_6 (purple).

content the migration energy decreases which is in agreement with the results of Deng *et al.*[53] The attractive interactions between the migrating Na^+ ion and the Si^{4+} substituents seem to lower the migration energy due to the stabilization of the transition state.

(ii) To determine the influence of the Na^+–Na^+ interactions on the migration energy, the amount of Na^+ near the migrating Na^+ ions was gradually increased in the structure $Na_1Zr_2P_3O_{12}$ ($x = 0$). The Na^+ positions adjacent to the migration pathway are depicted in Fig. S6,† and the resulting migration energies are shown in Fig. 8. There is no clear dependence of the migration energies on the number of Na^+ ions near the migration pathway. Again, our results agree with the findings of Deng *et al.* explaining the non-monotonic behaviour of migration energy in dependence on Na^+ concentration by a combination of local electrostatic repulsion and local charge imbalance.[53] In addition, our results show that the migration energies may depend on the arrangement of the Na^+ ions adjacent to the migration path as explained in detail in Section 5.2 in the ESI.† However, due to the large number of Na^+ sites in the lattice structure, it is not feasible to unambiguously describe the influence of Na^+ site occupation on the migration energy using DFT calculations.

(iii) During the migration, the Na^+ ions pass through different bottlenecks formed by three O^{2-} ions of SiO_4/PO_4 tetrahedra and ZrO_6 octahedra as illustrated in Fig. 9 for the 180° migration path. The bottlenecks A and A′ are located near the Na2 sites, while the bottlenecks B and B′ are located near the Na1 site.[68,83,85,90] The four different bottlenecks of the migration path are characterized by the size of their area.[90] As shown in Fig. S9,† bottleneck A is the smallest in most cases, consistent with the literature.[68,69,89,90] In all compositions the bottleneck areas A and A′ increase for $x = 3$ compared to $x = 0$ whereas B and B′ do not change. Larger bottlenecks may facilitate Na^+ ion migration resulting in lower migration energy.

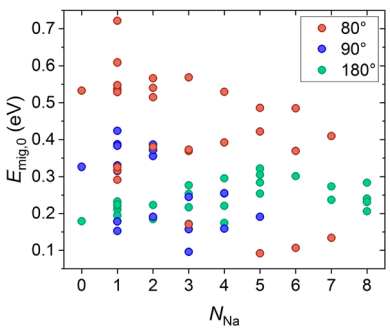

Fig. 8 Migration energy $E_{mig,0}$ of the pathways in 80° (red), 90° (blue) and 180° (green) dependent on the amount of Na^+ N_{Na^+} adjacent to the migration pathway in the structure with composition $Na_1Zr_2P_3O_{12}$.

In conclusion, our results show that (i) increasing Si^{4+} concentration lowers the migration energy $E_{mig,0}$ due to increasing attractive interactions of the migrating Na^+ ions and surrounding Si^{4+} ions stabilizing the transition state, (ii) there is no clear correlation between $E_{mig,0}$ and the repulsive interactions of the migrating Na^+ ions and surrounding Na^+ ions, and (iii) $E_{mig,0}$ may decreases with increasing size of the bottleneck areas A and A′.

5.2.3 Dependence on M-cations. The comparison of $E_{mig,0}$ of the compositions with different M-cations shows that $E_{mig,0}$ is similar for $M = Zr^{4+}$ (Fig. 6a) and $M = Hf^{4+}$ (Fig. 6b) but higher in $M = Sn^{4+}$ (Fig. 6c). The differences are largest at small substitution content x.

At small x, the Na^+–O^{2-} bond distances are smaller in $M = Sn^{4+}$ due to the smaller cell volume. Therefore, the fractional volume of the migrating Na^+ ions in $M = Sn^{4+}$ is smaller than in $M = Zr^{4+}$, Hf^{4+}, leading to higher steric hindrance and thus higher $E_{mig,0}$. However, at large x, there are no significant differences in the bond distances of the different compositions (Table S6†).

Moreover, the smaller cell volume in $M = Sn^{4+}$ leads to smaller bottlenecks (see Fig. S10†) which may also explain the higher migration energies $E_{mig,0}$ in accordance with the literature.[82,89,124] However, at high x, the differences in $E_{mig,0}$ are small and the results on the effect of the bottleneck on Na^+ migration behaviour must be interpreted with caution. Furthermore, Martinez-Juárez *et al.* have shown that the migration depends strongly on the size of the bottleneck only if it is smaller than the migrating ion, otherwise, it is influenced by the interactions between the migrating ion and the lattice.[124]

In addition, Sn^{4+} exhibits a different electronic structure than Zr^{4+}, Hf^{4+}, as mentioned above. The framework of the structures containing d^0 transition metals (Zr^{4+}, Hf^{4+}) is more

flexible compared to the one with d^{10} main-group elements (Sn^{4+}), and thus may better accommodate the migrating Na^+ ions resulting in lower $E_{mig,0}$.[117] Urban *et al.* have elucidated that d^0 transition metals tolerate site distortion with low energy costs.[125] The local geometry may be different depending on the electronic structure, which could additionally modify the geometry of the bottleneck.[119,120]

6 Investigation at the macroscopic level

KMC simulations were performed based on the DFT-derived energies from the previous section to clarify the influence of composition on Na^+ conductivity in $Na_{1+x}M_2Si_xP_{3-x}O_{12}$ with M = Zr^{4+}, Hf^{4+}, Sn^{4+} and $0.01 \leq x \leq 2.8$. As explained before, the simulations require knowledge of the configuration energies predicted by eqn (12) using pair interaction energies individually calculated and the migration energies determined by eqn (13) using the migration energies of the unsubstituted and fully substituted structure (Section 5.2).

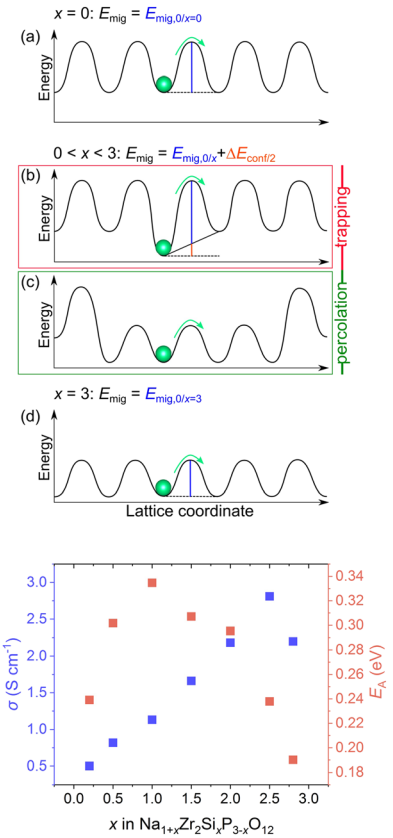

Fig. 10 (Top) Energy landscape of Na^+ positions and migration barrier E_{mig} in the lattice $Na_{1+x}M_2Si_xP_{3-x}O_{12}$ dependent on the substitution content x. (a) Non-substituted structure ($x = 0$) with uniform energy landscape, (b) low substituted structure where Na^+ ions are trapped in Si^{4+} rich environments, (c) high substituted structure where Na^+ ions percolate between Si^{4+} rich environments, (d) fully substituted structure ($x = 3$) with uniform energy landscape. (Bottom) Resulting ionic conductivity σ at 573 K and activation energy E_A in dependence of substitution content x in $Na_{1+x}Zr_2Si_xP_{3-x}O_{12}$. Values are taken from ref. 70.

In our previous study of $Na_{1+x}Zr_2Si_xP_{3-x}O_{12}$, we have already revealed the behaviour of the conductivity and the activation energy is strongly influenced by the local ionic environment of the Na^+ sites, as illustrated in Fig. 10.[70] The conductivities simulated at 573 K and activation energies of $Na_{1+x}Zr_2Si_xP_{3-x}O_{12}$ obtained in this earlier work are shown in the bottom plot of Fig. 10.[70] In the non-substituted structure the migration barrier E_{mig} only depends on the migration energy $E_{mig,0}$ as the energy landscape is uniform (Fig. 10a). However, due to the introduction of substituents, E_{mig} depends on the migration energy $E_{mig,0}$ and the configurational energy E_{conf} (Fig. 10b). At small x, Na^+ ions are trapped in low energy states near the introduced Si^{4+} ions due to favourable attractive interactions. The depth of the traps increases with the number of adjacent Si^{4+} leading to low conductivities and an increase in activation energy. But, with increasing x, percolation paths are formed due to the large number of Si^{4+} (Fig. 10c), which explains the increase in Na^+ conductivity and the decrease in the activation energy. In the fully substituted structure, the energy landscape is uniform and E_{mig} only depends on the migration energy $E_{mig,0}$ (Fig. 10d). Here, the activation energy is lowest, since $E_{mig,0}$ decreases with x. However, at very high substitution content, the number of vacant sodium sites is insufficient leading to a decrease in ionic conductivity.

In this study, we investigate the influence of different M-cations on the Na^+ diffusion behaviour in NaSICONs. The Na^+ ion conductivities, mobilities, and activation energies obtained from the KMC simulations are discussed below.

Fig. 11 shows the ionic conductivity dependent on x in $Na_{1+x}M_2Si_xP_{3-x}O_{12}$ with M = Zr^{4+}, Hf^{4+}, Sn^{4+}. As expected, the conductivity increases with temperature in all compositions. The conductivities of the compounds with M = Zr^{4+} (Fig. 11a) and M = Hf^{4+} (Fig. 11b) show similar dependence on x as explained above and differ only slightly at higher x due to small differences in the migration energy $E_{mig,0}$. In both structures, the maximum conductivity is reached at $x = 2.5$. For M = Sn^{4+} (Fig. 11c), the ionic conductivities are up to three orders of magnitude lower at small x in accordance with the literature.[89,120] In this structure, the attractive Na^+–Si^{4+} interactions are much stronger at small distances resulting in deeper traps of Na^+ ions, and the migration energies are higher at small x. The conductivity increases strongly at around $1.0 \leq x \leq 1.5$ due to the decrease in $E_{mig,0}$ and reaches the maximum at $2.0 \leq x \leq 2.5$. Compared to M = Zr^{4+}, Hf^{4+}, the maximum of conductivity is, first, lower by one order of magnitude because the Na^+ ions are trapped even at higher substitution levels. Second, the maximum shifts to lower substitution concentration due to the strong Na^+–Na^+ repulsion, leading to unfavourable Na^+ site energies and thus to a sharp decrease in conductivity.

In short, when comparing NaSICONs with different M-cations, the amplitude and maximum of the Na^+ conductivity are mainly determined by the Na^+–cation pair interactions. This hypothesis is verified by the results of KMC simulations, where the Na^+–cation pair interactions are not considered, as shown in Fig. S11.† Here, the conductivities of the composition with M = Sn^{4+} are only slightly lower compared to those of the composition with M = Zr^{4+}, Hf^{4+}, which is due to the higher migration energies $E_{mig,0}$.

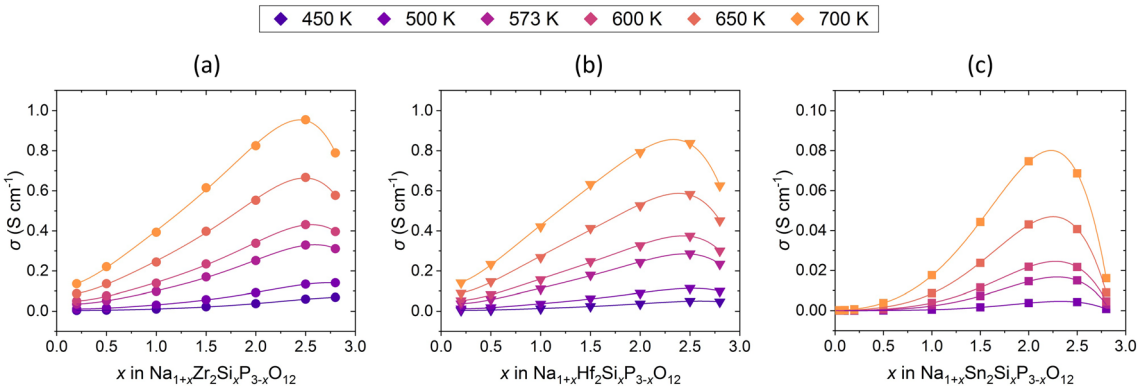

Fig. 11 Na^+ conductivity σ dependent on substitution content x of $Na_{1+x}M_2Si_xP_{3-x}O_{12}$ with (a) $M = Zr^{4+}$ ($0.2 \leq x \leq 2.8$), (b) $M = Hf^{4+}$ ($0.2 \leq x \leq 2.8$), (c) $M = Sn^{4+}$ ($0.01 \leq x \leq 2.8$) in $10 \times 10 \times 10$ cells in the temperature range of $450\ K \leq T \leq 700\ K$.

The comparison of conductivities obtained in this work and the total conductivities reported in the literature are shown in Fig. 12. The conductivities of compositions with $M = Zr^{4+}$ (Fig. 12a) and $M = Hf^{4+}$ (Fig. 12b) are in good agreement with experimental results at small and intermediate x, but are larger at high x and the maximum shifts to larger x values. However, the literature data scatter widely.[9,18,53] The total conductivity is composed of the bulk conductivity and the grain boundary conductivity, the latter being strongly influenced by the sample preparation process.[18,26,53,126] Poor microstructure, density, size of grains *etc.* lead to significantly low grain boundary conductivities, which determine the overall conductivity.[53,126] By

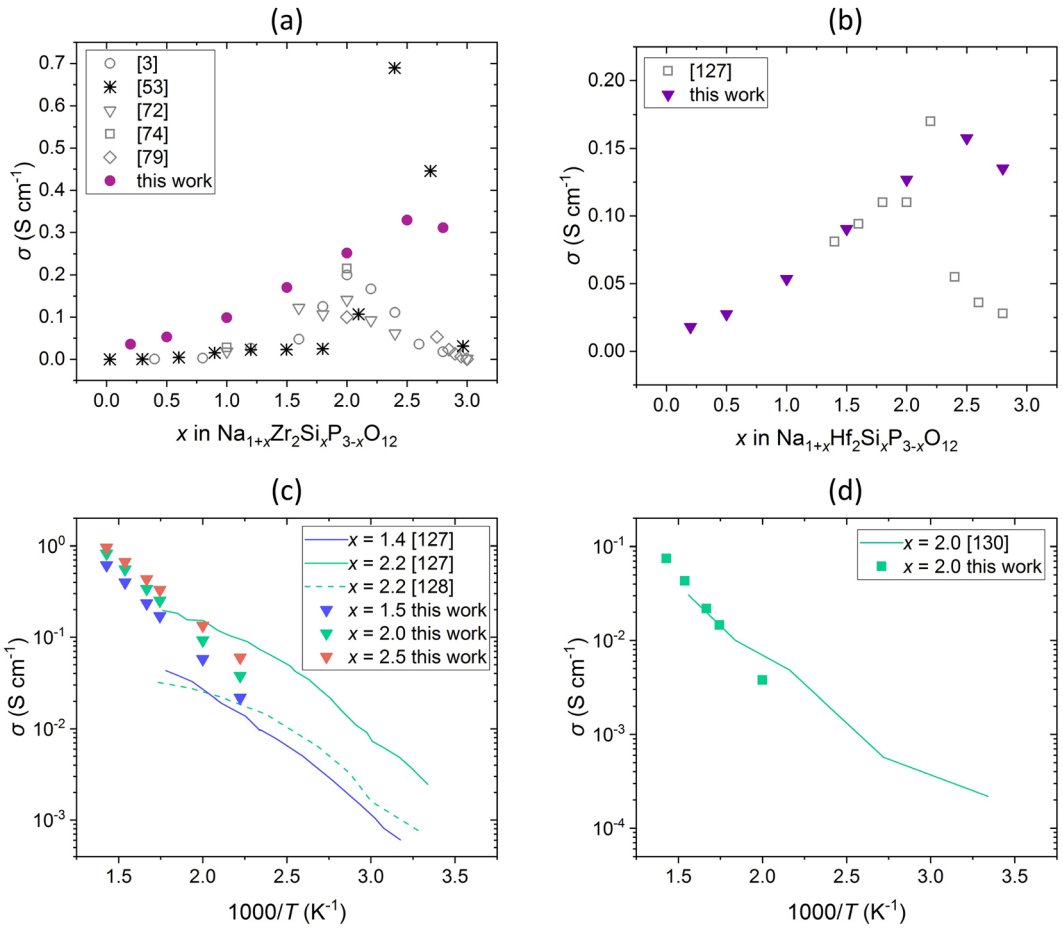

Fig. 12 Comparison of Na^+ conductivity σ in dependence on (a and b) substitution content x and (c and d) temperature T of $Na_{1+x}M_2Si_xP_{3-x}O_{12}$ with (a) $M = Zr^{4+}$, (b and c) $M = Hf^{4+}$, and (d) $M = Sn^{4+}$ in $10 \times 10 \times 10$ cells. Literature data of experimental studies[3,72,74,79,127,128,130] as well as KMC simulations[53] are shown.

optimizing the microstructure, and thus decreasing grain boundary resistance, the bulk conductivity gains influence and the total conductivity increases.[26,126] Ma *et al.* revealed that the total conductivity is largely underestimated in literature and reported high bulk conductivity of 1.5×10^{-2} S cm^{-1} at room temperature for substitution content of $x = 2.4$ when optimizing the microstructure, which is in agreement with our results.[26] It is also worth mentioning that the interpolated migration energies $E_{mig,0}$ may be underestimated at large x compared to $E_{mig,0}$ calculated with DFT, as shown in our previous study for $Na_{1+x}Zr_2Si_xP_{3-x}O_{12}$, and thus the conductivities may be overestimated.[70] However, the conductivities are in the same order of magnitude and the dependence on the substitution content is described accurately. A similar behaviour was found in a recent study by Deng *et al.* who investigated the ionic conductivity in $Na_{1+x}Zr_2Si_xP_{3-x}O_{12}$ using KMC simulations based on local-cluster expansion and DFT-NEB migration barriers.[53] Moreover, the simulated temperature dependence of the ionic conductivity of M = Hf^{4+} (Fig. 12c) and M = Sn^{4+} (Fig. 12d) agrees with experimental values. However, the values reported in different studies for the composition with M = Hf^{4+} and $x = 2.2$ also vary, which could be due to similar reasons as those discussed above.[127,128] Besides, similar conductivities for the compounds with M = Zr^{4+}, Hf^{4+} have been reported in previous studies, which coincide with our results.[6,120,123,127,129] Overall, the good agreement of our results with the literature data confirms the suitability of this method for studying conductivity in NaSICON-type structures.

Fig. 13 shows the Na^+ ion mobility in $Na_{1+x}M_2Si_xP_{3-x}O_{12}$ with M = Zr^{4+}, Hf^{4+}, Sn^{4+} dependent on the substitution level. In this way, the Na^+ ion diffusion behaviour is described without considering the increase of the charge carrier. Thus, the assumptions about the effects of the percolation paths formed by Si^{4+} and the low migration energy at high x are verified. The mobility shows a similar dependence on x as the conductivity. The maximum mobility is observed at $2.0 \leq x \leq 2.5$ in the compositions with M = Zr^{4+}, Hf^{4+} and at $x = 2$ in the composition with M = Sn^{4+}. The differences in the mobility are similar to those for conductivity and can be explained by the stronger attractive Na^+–Si^{4+} and repulsive Na^+–Na^+ interactions in the structure with M = Sn^{4+}, as described in detail above.

The temperature dependence of the ionic conductivities follows an Arrhenius behaviour (Fig. S12†). Fig. 14a shows the obtained activation energies E_A of all investigated $Na_{1+x}M_2Si_xP_{3-x}O_{12}$ compositions. In the non-substituted and fully substituted composition, E_A depends only on $E_{mig,0}$ as the energy landscape is uniform (see Fig. 10a and d). However, the introduction of

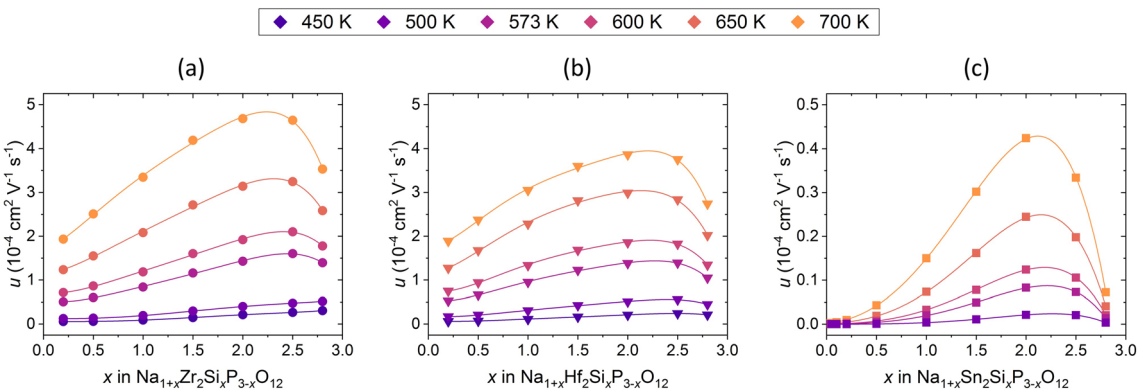

Fig. 13 Na^+ mobility u dependent on substitution content x of $Na_{1+x}M_2Si_xP_{3-x}O_{12}$ with (a) M = Zr^{4+} ($0.2 \leq x \leq 2.8$), (b) M = Hf^{4+} ($0.2 \leq x \leq 2.8$), (c) M = Sn^{4+} ($0.01 \leq x \leq 2.8$) in $10 \times 10 \times 10$ cells in the temperature range of 450 K $\leq T \leq$ 700 K.

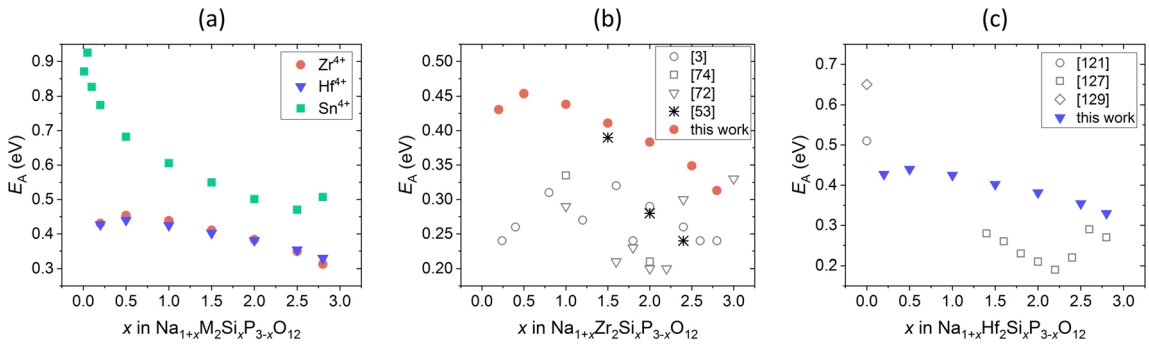

Fig. 14 (a) Activation energies E_A dependent on substitution content x of $Na_{1+x}M_2Si_xP_{3-x}O_{12}$ with M = Zr^{4+} ($0.2 \leq x \leq 2.8$) (red), Hf^{4+} ($0.2 \leq x \leq 2.8$) (blue), and Sn^{4+} ($0.01 \leq x \leq 2.8$) (green) obtained from Arrhenius plots (Fig. S12†). (b) Comparison of E_A of $Na_{1+x}Zr_2Si_xP_{3-x}O_{12}$ ($0.2 \leq x \leq 2.8$) (orange) with values obtained from experiments (grey)[3,72,74] and computational studies (black).[53] (c) Comparison of E_A of $Na_{1+x}Hf_2Si_xP_{3-x}O_{12}$ ($0.2 \leq x \leq 2.8$) (orange) with values obtained from experiments (grey).[120,127,129]

substituents leads to states with different energy (see Fig. 10b and c) and E_A depends also on the different cationic environments which are considered in the KMC simulations. As explained in Fig. 10, E_A is high at small x as Na^+ ions are trapped in low energy states. At higher x, E_A decreases because Na^+ ions percolate between favourable Si^{4+}-rich positions and the migration energy $E_{mig,0}$ decreases.

While E_A of the compositions $Na_{1+x}M_2Si_xP_{3-x}O_{12}$ with $M = Zr^{4+}$, Hf^{4+} are similar with a maximum around $x = 1.0$, E_A for $M = Sn^{4+}$ is much higher with a maximum at $x \approx 0.05$. This is due to stronger attractive Na^+–Si^{4+} interactions (see Fig. 5) which lead to more effective trapping even for small x. He *et al.* have elucidated that a locally flat energy landscape and low barriers of the high-energy site, *i.e.* the Na2 site, facilitates the concerted migration.[58] However, due to the stronger Na^+–Si^{4+} interactions in the structure with $M = Sn^{4+}$, which lowers the Na2 site energy, the local energy landscape becomes less uniform and the energy barriers increase, resulting in higher E_A. The E_A of all compositions and the differences between them decrease with increasing x, as the decreasing migration energies $E_{mig,0}$, which have the dominant impact, converge (see Fig. 6). Moreover, the energy landscape becomes more uniform with increasing Si^{4+} content, with the differences in Na^+–Si^{4+} interactions losing influence on the migration barrier and thus on E_A. At a high substitution level, E_A of the composition with $M = Sn^{4+}$ increases slightly caused by highly unfavourable repulsive Na^+–Na^+ interactions (see Fig. 4) which may increase the Na2 site energy strongly.

As shown in Fig. 14b, the activation energies of $Na_{1+x}Zr_2Si_xP_{3-x}O_{12}$ determined in this study are higher than those obtained from a.c. conductivity measurements and *ab initio* molecular dynamics simulations, especially at small substitution contents. However, the experimental values vary widely as discussed above. The calculated activation energies of $Na_{1+x}Hf_2Si_xP_{3-x}O_{12}$ are higher than the literature data at intermediate x and agree well at high x, as Fig. 14c shows. In general, the activation energies determined in this work are in reasonable accordance with the literature values. However, there are only a few or strongly fluctuating data in the literature, thus the comparison should be made with caution.

It can be concluded that the Na^+ transport properties mainly depend on the trapping of Na^+ by the introduced Si^{4+} at small x, the migration energy $E_{mig,0}$ at high x, and strong Na^+–Na^+ repulsion at very high x. The Na^+–cation interactions and thus the Na^+ transport properties can be influenced by the choice of M cations. Moreover, the ionic conductivity and mobility depend on the ratio of occupied to vacant sodium sites. Thus, our study points out that no simple correlation can be established to describe the ionic conductivity. The maximum of Na^+ mobility and conductivity is reached at a high substitution content of $2.0 \leq x \leq 2.5$ due to low migration energy and optimal ratio of unoccupied to occupied charge carrier sites.

7 Conclusion

We studied the influences of the Si^{4+} substitution concentration x, M-cation and temperature on Na^+ ion transport in the multi-element NaSICON-type structure $Na_{1+x}M_2Si_xP_{3-x}O_{12}$ ($M = Zr^{4+}$, Hf^{4+}, Sn^{4+} and $0 \leq x \leq 3$). Therefore, we combined accurate DFT calculations and KMC simulations for the investigation at both atomistic and macroscopic levels with affordable computational effort.

The DFT calculations show that the Na^+ site energy depends on Na^+–Na^+ interactions resulting mainly from electrostatic effects and Na^+–Si^{4+} interactions resulting from both electrostatic and elastic effects. Lower Na^+ and higher Si^{4+} content in the local environment leads to lower Na^+ site energy. However, the size and electronic structure of the M-cation must also be considered when describing the configurational energies. Smaller and more rigid MO_6 octahedra result in stronger pair interactions.

Moreover, we have shown that the migration energy $E_{mig,0}$ depends on various factors for different x: At low x, $E_{mig,0}$ is mainly influenced by the migration pathway. However, with increasing x, the ions adjacent to the migration path gain influence. $E_{mig,0}$ decreases with increasing Si^{4+} concentration because of favourable attractive interactions of the migrating Na^+ ions and surrounding Si^{4+} ions. In addition, the increasing size of the bottleneck may lower $E_{mig,0}$. Furthermore, $E_{mig,0}$ depends on the M-cation. The size of the M-cation affects the size of the bottleneck, and the electronic structure of the M-cation affects the flexibility of the structural framework. Smaller bottlenecks and more rigid MO_6 octahedra may increase $E_{mig,0}$ and could explain the highest values for compositions with $M = Sn^{4+}$.

Based on DFT-derived energies, we performed KMC simulations to investigate the macroscopic Na^+ conductivity. Using $Na_{1+x}M_2Si_xP_{3-x}O_{12}$ as an example, we showed that the Na^+ transport properties in NaSICON structures are determined by (i) the Na^+ trapping by introduced Si^{4+} at small x, (ii) the migration energy $E_{mig,0}$ at intermediate to high x, and (iii) the availability of vacant Na^+ site as well as the Na^+–Na^+ repulsion at very high x. Thus, the conductivity of compositions with $M = Zr^{4+}$, Hf^{4+} reaches the maximum at $x = 2.5$ due to percolation pathways formed by Si^{4+} rich environments, low $E_{mig,0}$ and optimal density of charge carrier sites. For the composition with $M = Sn^{4+}$, the ionic conductivities are significantly lower because of the stronger attractive Na^+–Si^{4+} interactions which form deeper traps for the Na^+ ions. In addition, the conductivity maximum is shifted to lower substitution concentrations of $2.0 \leq x \leq 2.5$ due to the stronger Na^+–Na^+ repulsion leading to unfavourable Na^+ site energies and thus to a sharp decrease in conductivity at high x.

The resulting activation energies depend on the local cationic environments of the Na^+ sites. E_A is high at small x because the Na^+ ions are trapped in low energy states, whereas E_A decreases at higher x due to the Na^+ percolation between favourable Si^{4+} rich positions as well as the decrease of $E_{mig,0}$. The activation energy of the composition with $M = Sn^{4+}$ is higher and the maximum appears at lower x compared to the compositions with $M = Zr^{4+}$ and Hf^{4+} because of the more effective trapping due to stronger attractive Na^+–Si^{4+} interactions.

Our results show that the Na^+ ion transport in NaSICONs can be modified by different cation substitution strategies in the host lattice $Na_1M_2PO_{12}$.

A rising number of Na^+ ions supports the correlated ionic migration as high energy sites are occupied, and also leads to an increase in ionic conductivity. One way to adjust the concentration of the Na^+ charge carrier is to incorporate excess Na^+ into the NaSICON compounds. Indeed, few studies have investigated the influences of excess Na^+ in NaSICONs[90,91,131–133] revealing that conductivity increases and activation energy decreases, based on the increase in Na^+ charge carrier[91,133] and enhanced mobility by the widening of the bottlenecks.[90,133]

The amount of Na^+ charge carrier can also be modified when the M^{4+} and P^{5+} sites are substituted with cations with various valence. As shown in this study, the substitution with subvalent cations leads not only to the increase in Na^+ concentration but also to the decrease in Na^+ ion migration energy due to the lower electrostatic repulsion with the migrating Na^+ ions. Therefore, the introduction of divalent or trivalent substituents could potentially further increase the Na^+ ion conductivity in NaSICONs. However, subvalent substituents could also cause a stronger trapping effect which in turn decreases the Na^+ ion mobility.

Furthermore, iso- and aliovalent substituents with bigger ionic sizes could enlarge the cell volume and thus the bottlenecks, possibly leading to an increase in Na^+ ion mobility.

Various studies have shown that the aliovalent substitution of M^{4+} by divalent cations, such as Mg^{2+},[22,66,134–138] Zn^{2+},[32,139,140] Co^{2+},[139] Ca^{2+},[29,141] and trivalent cations, such as In^{3+},[119,142,143] Sc^{3+},[92,119,143–147] Y^{3+},[139,140,143,148] La^{3+},[24,148] Pr^{3+}, Eu^{3+}, Lu^{3+},[149] improves the Na^+ mobility and conductivity due to an increase in Na^+ ions coupled with enhanced correlated Na^+ ion migration but also due to the modification of the phase purity and microstructure of the ceramics.

Based on our results, another way to optimize the Na^+ ion transport in NaSICONS could be to completely substitute P^{5+} ions by Si^{4+} ions while introducing M^{5+} ions to ensure that sufficient unoccupied Na^+ sites are available. Supervalent M-substitution in NaSICONs materials has been poorly investigated, but studies of $Na_{1+x-y}M_yZr_{2-y}Si_xP_{3-x}O_{12}$ with M^{5+} = V, Nb, Ta show promising conductivities up to 5.5×10^{-3} S cm^{-1} for $Na_{3.3}Zr_{1.9}Nb_{0.1}Si_{2.4}P_{0.6}O_{12}$.[135,140,150]

Additionally, the Na^+ ion mobility can be influenced by Na^+–cation interactions, which are determined by the valence electron configuration of the M cations. In this study, we have shown that d^0 valence orbitals induce weaker Na^+–cation interactions compared to d^{10} valence orbitals, resulting in weaker Na^+ ion trapping and thus higher Na^+ ion mobility. Thus, the introduction of M cations exhibiting d^0 valence electron configuration, such as Mg^{2+}, Sc^{3+}, Ce^{4+}, V^{5+}, appears to provide a sound strategy to optimize the Na^+ ion mobility.

In summary, the method proposed in this study is suitable to investigate various NaSCION compositions over large length and time scales with low computational effort. Our results provide a comprehensive explanation of the Na^+ diffusion behaviour in NaSICONs to optimize the ionic conductivity.

Conflicts of interest

There are no conflicts to declare.

Acknowledgements

The authors gratefully acknowledge the computing time provided to them at the NHR Center NHR4CES at RWTH Aachen University (project number p0020107). This is funded by the Federal Ministry of Education and Research, and the state governments participating on the basis of the resolutions of the GWK for national high-performance computing at universities (https://www.nhr-verein.de/unsere-partner).

References

1 L.-O. Hagman, P. Kierkegaard, P. Karvonen, A. I. Virtanen and J. Paasivirta, The crystal structure of $NaMe_2^{IV}(PO_4)_3$; Me^{IV}=Ge, Ti, Zr, *Acta Chem. Scand.*, 1968, **22**, 1822–1832.
2 H.-P. Hong, Crystal structures and crystal chemistry in the system $Na_{1+x}Zr_2Si_xP_{3-x}O_{12}$, *Mater. Res. Bull.*, 1976, **11**, 173–182.
3 J. B. Goodenough, H.-P. Hong and J. A. Kafalas, Fast Na^+-ion transport in skeleton structures, *Mater. Res. Bull.*, 1976, **11**, 203–220.
4 J. Alamo and R. Roy, Crystal chemistry of the $NaZr_2(PO_4)_3$, NZP or CTP, structure family, *J. Mater. Sci.*, 1986, **21**, 444–450.
5 N. Anantharamulu, K. Koteswara Rao, G. Rambabu, B. Vijaya Kumar, V. Radha and M. Vithal, A wide-ranging review on NASICON type materials, *J. Mater. Sci.*, 2011, **46**, 2821–2837.
6 M. Guin and F. Tietz, Survey of the transport properties of sodium superionic conductor materials for use in sodium batteries, *J. Power Sources*, 2015, **273**, 1056–1064.
7 R. Rajagopalan, Z. Zhang, Y. Tang, C. Jia, X. Ji and H. Wang, Understanding crystal structures, ion diffusion mechanisms and sodium storage behaviors of NASICON materials, *Energy Storage Mater.*, 2021, **34**, 171–193.
8 Z. Yang, B. Tang, Z. Xie and Z. Zhou, NASICON-type $Na_3Zr_2Si_2PO_{12}$ solid-state electrolytes for sodium batteries, *ChemElectroChem*, 2021, **8**, 1035–1047.
9 Y. B. Rao, K. K. Bharathi and L. N. Patro, Review on the synthesis and doping strategies in enhancing the Na ion conductivity of $Na_3Zr_2Si_2PO_{12}$ (NASICON) based solid electrolytes, *Solid State Ionics*, 2021, **366**, 115671.
10 C. Li, R. Li, K. Liu, R. Si, Z. Zhang and Y.-S. Hu, NASICON: A promising solid electrolyte for solid-state sodium batteries, *Interdiscip. Mater.*, 2022, **1**, 396–416.
11 L. Zhang, Y. Liu, Y. You, A. Vinu and L. Mai, NASICONs-type solid-state electrolytes: The history, physicochemical properties, and challenges, *Interdiscip. Mater.*, 2022, **2**, 91–110.
12 K. Singh, A. Chakraborty, R. Thirupathi and S. Omar, Recent advances in NASICON-type oxide electrolytes for solid-state sodium-ion rechargeable batteries, *Ionics*, 2022, **28**, 1–31.

13 C. Jiang, H. Li and C. Wang, Recent progress in solid-state electrolytes for alkali-ion batteries, *Sci. Bull.*, 2017, **62**, 1473–1490.
14 W. Hou, X. Guo, X. Shen, K. Amine, H. Yu and J. Lu, Solid electrolytes and interfaces in all-solid-state sodium batteries: Progress and perspective, *Nano Energy*, 2018, **52**, 279–291.
15 C. Zhao, L. Liu, X. Qi, Y. Lu, F. Wu, J. Zhao, Y. Yu, Y.-S. Hu and L. Chen, Solid-state sodium batteries, *Adv. Energy Mater.*, 2018, **8**, 1703012.
16 C. Zhou, S. Bag and V. Thangadurai, Engineering materials for progressive all-solid-state Na batteries, *ACS Energy Lett.*, 2018, **3**, 2181–2198.
17 L. Fan, S. Wei, S. Li, Q. Li and Y. Lu, Recent progress of the solid-state electrolytes for high-energy metal-based batteries, *Adv. Energy Mater.*, 2018, **8**, 1702657.
18 Q. Ma and F. Tietz, Solid-state electrolyte materials for sodium batteries: Towards practical applications, *ChemElectroChem*, 2020, **7**, 2693–2713.
19 V. Thangadurai and B. Chen, Solid Li-and Na-ion electrolytes for next generation rechargeable batteries, *Chem. Mater.*, 2022, **34**, 6637–6658.
20 Y. Noguchi, E. Kobayashi, L. S. Plashnitsa, S. Okada and J. Yamaki, Fabrication and performances of all solid-state symmetric sodium battery based on NASICON-related compounds, *Electrochim. Acta*, 2013, **101**, 59–65.
21 F. Lalère, J.-B. Leriche, M. Courty, S. Boulineau, V. Viallet, C. Masquelier and V. Seznec, An all-solid state NASICON sodium battery operating at 200°C, *J. Power Sources*, 2014, **247**, 975–980.
22 S. Song, H. M. Duong, A. M. Korsunsky, N. Hu and L. Lu, A Na^+ superionic conductor for room-temperature sodium batteries, *Sci. Rep.*, 2016, **6**, 1–10.
23 W. Zhou, Y. Li, S. Xin and J. B. Goodenough, Rechargeable sodium all-solid-state battery, *ACS Cent. Sci.*, 2017, **3**, 52–57.
24 Z. Zhang, Q. Zhang, J. Shi, Y. S. Chu, X. Yu, K. Xu, M. Ge, H. Yan, W. Li and L. Gu, A self-forming composite electrolyte for solid-state sodium battery with ultralong cycle life, *Adv. Energy Mater.*, 2017, **7**, 1601196.
25 T. Lan, C.-L. Tsai, F. Tietz, X.-K. Wei, M. Heggen, R. E. Dunin-Borkowski, R. Wang, Y. Xiao, Q. Ma and O. Guillon, Room-temperature all-solid-state sodium batteries with robust ceramic interface between rigid electrolyte and electrode materials, *Nano Energy*, 2019, **65**, 104040.
26 Q. Ma, C.-L. Tsai, X.-K. Wei, M. Heggen, F. Tietz and J. T. S. Irvine, Room temperature demonstration of a sodium superionic conductor with grain conductivity in excess of 0.01 S cm^{-1} and its primary applications in symmetric battery cells, *J. Mater. Chem. A*, 2019, **7**, 7766–7776.
27 P. Kehne, C. Guhl, Q. Ma, F. Tietz, L. Alff, R. Hausbrand and P. Komissinskiy, Electrochemical performance of all-solid-state sodium-ion model cells with crystalline Na_xCoO_2 thin-film cathodes, *J. Electrochem. Soc.*, 2019, **166**, A5328.
28 P. Kehne, C. Guhl, Q. Ma, F. Tietz, L. Alff, R. Hausbrand and P. Komissinskiy, Sc-substituted NASICON solid electrolyte for an all-solid-state Na_xCoO_2/Nasicon/Na sodium model battery with stable electrochemical performance, *J. Power Sources*, 2019, **409**, 86–93.
29 Y. Lu, J. A. Alonso, Q. Yi, L. Lu, Z. L. Wang and C. Sun, A high-performance monolithic solid-state sodium battery with Ca^{2+} doped $Na_3Zr_2Si_2PO_{12}$ electrolyte, *Adv. Energy Mater.*, 2019, **9**, 1901205.
30 E. Matios, H. Wang, C. Wang, X. Hu, X. Lu, J. Luo and W. Li, Graphene regulated ceramic electrolyte for solid-state sodium metal battery with superior electrochemical stability, *ACS Appl. Mater. Interfaces*, 2019, **11**, 5064–5072.
31 Z. Zhang, S. Wenzel, Y. Zhu, J. Sann, L. Shen, J. Yang, X. Yao, Y.-S. Hu, C. Wolverton and H. Li, $Na_3Zr_2Si_2PO_{12}$: A stable Na^+-ion solid electrolyte for solid-state batteries, *ACS Appl. Energy Mater.*, 2020, **3**, 7427–7437.
32 J. Yang, G. Liu, M. Avdeev, H. Wan, F. Han, L. Shen, Z. Zou, S. Shi, Y.-S. Hu and C. Wang, Ultrastable all-solid-state sodium rechargeable batteries, *ACS Energy Lett.*, 2020, **5**, 2835–2841.
33 X. Wang, W. Mei, J. Chen, D. Wang and Z. Mao, Rare earth oxide-assisted sintered NASICON electrolyte composed of a phosphate grain boundary phase with low electronic conductivity, *ACS Appl. Energy Mater.*, 2021, **5**, 777–783.
34 B. Dunn, H. Kamath and J.-M. Tarascon, Electrical energy storage for the grid: A battery of choices, *Science*, 2011, **334**, 928–935.
35 B. L. Ellis and L. F. Nazar, Sodium and sodium-ion energy storage batteries, *Curr. Opin. Solid State Mater. Sci.*, 2012, **16**, 168–177.
36 V. Palomares, P. Serras, I. Villaluenga, K. B. Hueso, J. Carretero-González and T. Rojo, Na-ion batteries, recent advances and present challenges to become low cost energy storage systems, *Energy Environ. Sci.*, 2012, **5**, 5884–5901.
37 M. D. Slater, D. Kim, E. Lee and C. S. Johnson, Sodium-ion batteries, *Adv. Funct. Mater.*, 2013, **23**, 947–958.
38 H. Pan, Y.-S. Hu and L. Chen, Room-temperature stationary sodium-ion batteries for large-scale electric energy storage, *Energy Environ. Sci.*, 2013, **6**, 2338–2360.
39 S. Y. Hong, Y. Kim, Y. Park, A. Choi, N.-S. Choi and K. T. Lee, Charge carriers in rechargeable batteries: Na ions *vs.* Li ions, *Energy Environ. Sci.*, 2013, **6**, 2067–2081.
40 N. Yabuuchi, K. Kubota, M. Dahbi and S. Komaba, Research development on sodium-ion batteries, *Chem. Rev.*, 2014, **114**, 11636–11682.
41 D. Larcher and J.-M. Tarascon, Towards greener and more sustainable batteries for electrical energy storage, *Nat. Chem.*, 2015, **7**, 19–29.
42 D. Kundu, E. Talaie, V. Duffort and L. F. Nazar, The emerging chemistry of sodium ion batteries for electrochemical energy storage, *Angew. Chem., Int. Ed.*, 2015, **54**, 3431–3448.
43 J.-Y. Hwang, S.-T. Myung and Y.-K. Sun, Sodium-ion batteries: Present and future, *Chem. Soc. Rev.*, 2017, **46**, 3529–3614.

44 C. Vaalma, D. Buchholz, M. Weil and S. Passerini, A cost and resource analysis of sodium-ion batteries, *Nat. Rev. Mater.*, 2018, **3**, 1–11.
45 C. Delmas, Sodium and sodium-ion batteries: 50 years of research, *Adv. Energy Mater.*, 2018, **8**, 1703137.
46 L. Chen, M. Fiore, J. E. Wang, R. Ruffo, D.-K. Kim and G. Longoni, Readiness level of sodium-ion battery technology: A materials review, *Adv. Sustainable Syst.*, 2018, **2**, 1700153.
47 T. Liu, Y. Zhang, Z. Jiang, X. Zeng, J. Ji, Z. Li, X. Gao, M. Sun, Z. Lin and M. Ling, Exploring competitive features of stationary sodium ion batteries for electrochemical energy storage, *Energy Environ. Sci.*, 2019, **12**, 1512–1533.
48 Y. E. Durmus, H. Zhang, F. Baakes, G. Desmaizieres, H. Hayun, L. Yang, M. Kolek, V. Küpers, J. Janek and D. Mandler, Side by side battery technologies with lithium-ion based batteries, *Adv. Energy Mater.*, 2020, **10**, 2000089.
49 H. Che, S. Chen, Y. Xie, H. Wang, K. Amine, X.-Z. Liao and Z.-F. Ma, Electrolyte design strategies and research progress for room-temperature sodium-ion batteries, *Energy Environ. Sci.*, 2017, **10**, 1075–1101.
50 T. Famprikis, P. Canepa, J. A. Dawson, M. S. Islam and C. Masquelier, Fundamentals of inorganic solid-state electrolytes for batteries, *Nat. Mater.*, 2019, **18**, 1278–1291.
51 D. H. S. Tan, A. Banerjee, Z. Chen and Y. S. Meng, From nanoscale interface characterization to sustainable energy storage using all-solid-state batteries, *Nat. Nanotechnol.*, 2020, **15**, 170–180.
52 Y. Wang, S. Song, C. Xu, N. Hu, J. Molenda and L. Lu, Development of solid-state electrolytes for sodium-ion battery–A short review, *NanoMater. Sci.*, 2019, **1**, 91–100.
53 Z. Deng, T. P. Mishra, E. Mahayoni, Q. Ma, A. J. K. Tieu, O. Guillon, J.-N. Chotard, V. Seznec, A. K. Cheetham and C. Masquelier, Fundamental investigations on the sodium-ion transport properties of mixed polyanion solid-state battery electrolytes, *Nat. Commun.*, 2022, **13**, 1–14.
54 Y. Gao, A. M. Nolan, P. Du, Y. Wu, C. Yang, Q. Chen, Y. Mo and S.-H. Bo, Classical and emerging characterization techniques for investigation of ion transport mechanisms in crystalline fast ionic conductors, *Chem. Rev.*, 2020, **120**, 5954–6008.
55 P. Canepa, Pushing forward simulation techniques of ion transport in ion conductors for energy materials, *ACS Mater. Au*, 2023, **3**, 75–82.
56 M. Bianchini, V. Lacivita, D.-H. Seo and H. Kim, Advances and challenges in multiscale characterizations and analyses for battery materials, *J. Mater. Res.*, 2022, **37**, 1–17.
57 A. van der Ven, Z. Deng, S. Banerjee and S. P. Ong, Rechargeable alkali-ion battery materials: Theory and computation, *Chem. Rev.*, 2020, **120**, 6977–7019.
58 X. He, Y. Zhu and Y. Mo, Origin of fast ion diffusion in super-ionic conductors, *Nat. Commun.*, 2017, **8**, 1–7.
59 B. Ouyang, J. Wang, T. He, C. J. Bartel, H. Huo, Y. Wang, V. Lacivita, H. Kim and G. Ceder, Synthetic accessibility and stability rules of NASICONs, *Nat. Commun.*, 2021, **12**, 1–11.
60 P. P. Kumar and S. Yashonath, A full interionic potential for $Na_{1+x}Zr_2Si_xP_{3-x}O_{12}$ superionic conductors, *J. Am. Chem. Soc.*, 2002, **124**, 3828–3829.
61 P. P. Kumar and S. Yashonath, Structure, conductivity, and ionic motion in $Na_{1+x}Zr_2Si_xP_{3-x}O_{12}$: A simulation study, *J. Phys. Chem. B*, 2002, **106**, 7081–7089.
62 S. Roy and P. Padma Kumar, Framework flexibility of sodium zirconium phosphate: Role of disorder, and polyhedral distortions from Monte Carlo investigation, *J. Mater. Sci.*, 2012, **47**, 4946–4954.
63 S. Roy and P. P. Kumar, Influence of Si/P ordering on Na^+ transport in NASICONs, *Phys. Chem. Chem. Phys.*, 2013, **15**, 4965–4969.
64 S. Roy and P. P. Kumar, Influence of cationic ordering on ion transport in NASICONs: Molecular dynamics study, *Solid State Ionics*, 2013, **253**, 217–222.
65 K. M. Bui, D. an van, S. Okada and T. Ohno, Na-ion diffusion in a NASICON-type solid electrolyte: A density functional study, *Phys. Chem. Chem. Phys.*, 2016, **18**, 27226–27231.
66 Z. Zhang, Z. Zou, K. Kaup, R. Xiao, S. Shi, M. Avdeev, Y.-S. Hu, D. Wang, B. He and H. Li, Correlated migration invokes higher Na^+-ion conductivity in NASICON-type solid electrolytes, *Adv. Energy Mater.*, 2019, **9**, 1902373.
67 Z. Deng, G. Sai Gautam, S. K. Kolli, J.-N. Chotard, A. K. Cheetham, C. Masquelier and P. Canepa, Phase behavior in rhombohedral NASICON electrolytes and electrodes, *Chem. Mater.*, 2020, **32**, 7908–7920.
68 Z. Zou, N. Ma, A. Wang, Y. Ran, T. Song, Y. Jiao, J. Liu, H. Zhou, W. Shi and B. He, Relationships between Na^+ distribution, concerted migration, and diffusion properties in rhombohedral NASICON, *Adv. Energy Mater.*, 2020, **10**, 2001486.
69 Z. Zou, N. Ma, A. Wang, Y. Ran, T. Song, B. He, A. Ye, P. Mi, L. Zhang and H. Zhou, Identifying migration channels and bottlenecks in monoclinic NASICON-type solid electrolytes with hierarchical ion-transport algorithms, *Adv. Funct. Mater.*, 2021, **31**, 2107747.
70 J. Schuett, F. Pescher and S. Neitzel-Grieshammer, The origin of high Na^+ ion conductivity in $Na_{1+x}Zr_2Si_xP_{3-x}O_{12}$ NASICON materials, *Phys. Chem. Chem. Phys.*, 2022, **24**, 22154–22167.
71 M. Avdeev, Crystal chemistry of NASICONs: Ideal framework, distortion, and connection to properties, *Chem. Mater.*, 2021, **33**, 7620–7632.
72 J. P. Boilot, J. P. Salanie, G. Desplanches and D. Le Potier, Phase transformation in $Na_{1+x}Si_xZr_2P_{3-x}O_{12}$ compounds, *Mater. Res. Bull.*, 1979, **14**, 1469–1477.
73 J.-J. Didisheim, E. Prince and B. J. Wuensch, Neutron Rietveld analysis of structural changes in NASICON solid solutions $Na_{1+x}Zr_2Si_xP_{3-x}O_{12}$ at elevated temperatures: $x = 1.6$ and 2.0 at 320 °C, *Solid State Ionics*, 1986, **18**, 944–958.
74 W. H. Baur, J. R. Dygas, D. H. Whitmore and J. Faber, Neutron powder diffraction study and ionic conductivity of $Na_2Zr_2SiP_2O_{12}$ and $Na_3Zr_2Si_2PO_{12}$, *Solid State Ionics*, 1986, **18**, 935–943.

75 J. P. Boilot, G. Collin and P. Colomban, Crystal structure of the true NASICON: $Na_3Zr_2Si_2PO_{12}$, *Mater. Res. Bull.*, 1987, **22**, 669–676.
76 J.-P. Boilot, G. Collin and P. Colomban, Relation structure-fast ion conduction in the NASICON solid solution, *J. Solid State Chem.*, 1988, **73**, 160–171.
77 U. von Alpen, M. F. Bell and W. Wichelhaus, Phase transition in NASICON ($Na_3Zr_2Si_2PO_{12}$), *Mater. Res. Bull.*, 1979, **14**, 1317–1322.
78 T. Feist, P. K. Davies and E. Vogel, The energetics of phase transitions in the system $Na_{1+x}Zr_2Si_xP_{3-x}O12$, $1.9 \leq x \leq 2.5$, *Thermochim. Acta*, 1986, **106**, 57–61.
79 D. T. Qui, J. J. Capponi, J. C. Joubert and R. D. Shannon, Crystal structure and ionic conductivity in $Na_4Zr_2Si_3O_{12}$, *J. Solid State Chem.*, 1981, **39**, 219–229.
80 C. Delmas, R. Olazcuaga, G. Le Flem, P. Hagenmuller, F. Cherkaoui and R. Brochu, Crystal chemistry of the $Na_{1+x}Zr_{2-x}L_x(PO_4)_3$ (L=Cr, In, Yb) solid solutions, *Mater. Res. Bull.*, 1981, **16**, 285–290.
81 B. J. Wuensch, L. J. Schioler and E. Prince, Relation between structure and conductivity in the NASICON solid solution system, *High Temp. Solid Oxide Electrolytes*, 1983, **2**, 59–74.
82 J. J. Shi, G. Q. Yin, L. M. Jing, J. Guan, M. P. Wu, Y. L. Zhou, H. L. Lou and Z. Wang, Lithium and sodium diffusion in solid electrolyte materials of $AM_2(PO_4)_3$ (A=Li, Na, M=Ti, Sn and Zr), *Int. J. Mod. Phys. B*, 2014, **28**, 1450176.
83 F. Cherkaoui, G. Villeneuve, C. Delmas and P. Hagenmuller, Sodium motion in the NASICON related $Na_{1+x}Zr_{2-x}In_x(PO_4)_3$ solid solution: An NMR study, *J. Solid State Chem.*, 1986, **65**, 293–300.
84 H. Kohler, H. Schulz and O. Melnikov, Composition and conduction mechanism of the NASICON structure X-ray diffraction study on two crystals at different temperatures, *Mater. Res. Bull.*, 1983, **18**, 1143–1152.
85 H. Kohler and H. Schulz, NASICON solid electrolytes part I: The Na^+-diffusion path and its relation to the structure, *Mater. Res. Bull.*, 1985, **20**, 1461–1471.
86 H. Kohler and H. Schulz, NASICON solid electrolytes part II-X-ray diffraction experiments on sodium-zirconium-phosphate single crystals at 295K and at 993K, *Mater. Res. Bull.*, 1986, **21**, 23–31.
87 S. H. Jacobson, M. A. Ratner and A. Nitzan, Stoichiometry-dependent conductivity in framework ionic conductors, *Phys. Rev. B: Condens. Matter Mater. Phys.*, 1981, **23**, 1580.
88 S. H. Jacobson, A. Nitzan and M. A. Ratner, A stochastic Langevin dynamics study of correlated ionic motion in one dimensional solid electrolytes, *J. Chem. Phys.*, 1980, **72**, 3712–3719.
89 E. R. Losilla, M. A. G. Aranda, S. Bruque, M. A. París, J. Sanz and A. R. West, Understanding Na mobility in NASICON materials: A Rietveld, 23Na and 31P MAS NMR, and impedance study, *Chem. Mater.*, 1998, **10**, 665–673.
90 H. Park, K. Jung, M. Nezafati, C.-S. Kim and B. Kang, Sodium ion diffusion in Nasicon ($Na_3Zr_2Si_2PO_{12}$) solid electrolytes: Effects of excess sodium, *ACS Appl. Mater. Interfaces*, 2016, **8**, 27814–27824.
91 S. Naqash, F. Tietz, E. Yazhenskikh, M. Müller and O. Guillon, Impact of sodium excess on electrical conductivity of $Na_3Zr_2Si_2PO_{12}$+xNa_2O ceramics, *Solid State Ionics*, 2019, **336**, 57–66.
92 Q. Ma, M. Guin, S. Naqash, C.-L. Tsai, F. Tietz and O. Guillon, Scandium-substituted $Na_3Zr_2(SiO_4)_2(PO_4)$ prepared by a solution-assisted solid-state reaction method as sodium-ion conductors, *Chem. Mater.*, 2016, **28**, 4821–4828.
93 P. Hohenberg and W. Kohn, Inhomogeneous electron gas, *Phys. Rev.*, 1964, **136**, B864.
94 W. Kohn and L. J. Sham, Self-consistent equations including exchange and correlation effects, *Phys. Rev.*, 1965, **140**, A1133.
95 G. Kresse and J. Hafner, Ab initio molecular dynamics for liquid metals, *Phys. Rev. B: Condens. Matter Mater. Phys.*, 1993, **47**, 558.
96 G. Kresse and J. Hafner, Norm-conserving and ultrasoft pseudopotentials for first-row and transition elements, *J. Phys.: Condens. Matter*, 1994, **6**, 8245.
97 G. Kresse and J. Furthmüller, Efficiency of *ab initio* total energy calculations for metals and semiconductors using a plane-wave basis set, *Comput. Mater. Sci.*, 1996, **6**, 15–50.
98 G. Kresse and J. Furthmüller, Efficient iterative schemes for *ab initio* total-energy calculations using a plane-wave basis set, *Phys. Rev. B: Condens. Matter Mater. Phys.*, 1996, **54**, 11169.
99 J. P. Perdew, K. Burke and M. Ernzerhof, Generalized gradient approximation made simple, *Phys. Rev. Lett.*, 1996, **77**, 3865.
100 P. E. Blöchl, Projector augmented-wave method, *Phys. Rev. B: Condens. Matter Mater. Phys.*, 1994, **50**, 17953.
101 H. J. Monkhorst and J. D. Pack, Special points for Brillouin-zone integrations, *Phys. Rev. B: Condens. Matter Mater. Phys.*, 1976, **13**, 5188.
102 S. Baroni, P. Giannozzi and A. Testa, Green's-function approach to linear response in solids, *Phys. Rev. Lett.*, 1987, **58**, 1861.
103 S. Baroni, S. de Gironcoli, A. Dal Corso and P. Giannozzi, Phonons and related crystal properties from density-functional perturbation theory, *Rev. Mod. Phys.*, 2001, **73**, 515.
104 M. Gajdoš, K. Hummer, G. Kresse, J. Furthmüller and F. Bechstedt, Linear optical properties in the projector-augmented wave methodology, *Phys. Rev. B: Condens. Matter Mater. Phys.*, 2006, **73**, 45112.
105 H. Jónsson, G. Mills and K. W. Jacobsen, in *Classical and Quantum Dynamics in Condensed Phase Simulations*, World Scientific, 1998, pp. 385–404.
106 G. Henkelman, B. P. Uberuaga and H. Jónsson, A climbing image nudged elastic band method for finding saddle points and minimum energy paths, *J. Chem. Phys.*, 2000, **113**, 9901–9904.
107 G. Henkelman and H. Jónsson, Improved tangent estimate in the nudged elastic band method for finding minimum energy paths and saddle points, *J. Chem. Phys.*, 2000, **113**, 9978–9985.

108 C. C. Battaile, The kinetic Monte Carlo method: Foundation, implementation, and application, *Comput. Methods Appl. Mech. Eng.*, 2008, **197**, 3386–3398.
109 S. Eisele and S. Grieshammer, MOCASSIN: Metropolis and kinetic Monte Carlo for solid electrolytes, *J. Comput. Chem.*, 2020, **41**, 2663–2677.
110 A. van der Ven, G. Ceder, M. Asta and P. D. Tepesch, First-principles theory of ionic diffusion with nondilute carriers, *Phys. Rev. B: Condens. Matter Mater. Phys.*, 2001, **64**, 184307.
111 G. H. Vineyard, Frequency factors and isotope effects in solid state rate processes, *J. Phys. Chem. Solids*, 1957, **3**, 121–127.
112 A. van der Ven, J. C. Thomas, B. Puchala and A. R. Natarajan, First-principles statistical mechanics of multicomponent crystals, *Annu. Rev. Mater. Res.*, 2018, **48**, 27–55.
113 R. D. Shannon, Revised effective ionic radii and systematic studies of interatomic distances in halides and chalcogenides, *Acta Crystallogr., Sect. A: Cryst. Phys., Diffr., Theor. Gen. Crystallogr.*, 1976, **32**, 751–767.
114 A. Bogicevic and C. Wolverton, Nature and strength of defect interactions in cubic stabilized zirconia, *Phys. Rev. B: Condens. Matter Mater. Phys.*, 2003, **67**, 24106.
115 D. A. Andersson, S. I. Simak, N. V. Skorodumova, I. A. Abrikosov and B. Johansson, Optimization of ionic conductivity in doped ceria, *Proc. Natl. Acad. Sci. U. S. A.*, 2006, **103**, 3518–3521.
116 S. Grieshammer, B. O. H. Grope, J. Koettgen and M. Martin, A combined DFT+U and Monte Carlo study on rare earth doped ceria, *Phys. Chem. Chem. Phys.*, 2014, **16**, 9974–9986.
117 J. L. Rodrigo and J. Alamo, Phase transition in $NaSn_2(PO_4)_3$ and thermal expansion of $NaM_2^{IV}(PO_4)_3$; M^{IV}=Ti, Sn, Zr, *Mater. Res. Bull.*, 1991, **26**, 475–480.
118 P. Tarte, A. Rulmont and C. Merckaert-Ansay, Vibrational spectrum of NASICON-like, rhombohedral orthophosphates $M^IM^{IV}{}_2(PO_4)_3$, *Spectrochim. Acta, Part A*, 1986, **42**, 1009–1016.
119 J. M. Winand, A. Rulmont and P. Tarte, Ionic conductivity of the $Na_{1+x}M_x^{III}Zr_{2-x}(PO_4)_3$ systems (M=Al, Ga, Cr, Fe, Sc, In, Y, Yb), *J. Mater. Sci.*, 1990, **25**, 4008–4013.
120 J.-M. Winand, A. Rulmont and P. Tarte, Nouvelles solutions solides $L^I(M^{IV})_{2-x}(N^{IV})_x(PO_4)_3$ (L=Li, Na M, N=Ge, Sn, Ti, Zr, Hf) synthèse et étude par diffraction x et conductivité ionique, *J. Solid State Chem.*, 1991, **93**, 341–349.
121 J. Alamo, Chemistry and properties of solids with the [NZP] skeleton, *Solid State Ionics*, 1993, **63**, 547–561.
122 M. P. Carrasco, M. C. Guillem and J. Alamo, Synthesis and structural study of $NaTi_2(PO_4)_3$-$NaSn_2(PO_4)_3$ solid solutions. I. The effect of composition on lattice parameters, *Mater. Res. Bull.*, 1992, **27**, 603–610.
123 R. J. Cava, E. M. Vogel and D. W. Johnson Jr, Effect of homovalent framework cation substitutions on the sodium ion conductivity in $Na_3Zr_2Si_2PO_{12}$, *J. Am. Ceram. Soc.*, 1982, **65**, c157–c159.
124 A. Martinez-Juarez, C. Pecharromán, J. E. Iglesias and J. M. Rojo, Relationship between activation energy and bottleneck size for Li^+ ion conduction in NASICON materials of composition $LiMM'(PO_4)_3$; M, M'=Ge, Ti, Sn, Hf, *J. Phys. Chem. B*, 1998, **102**, 372–375.
125 A. Urban, A. Abdellahi, S. Dacek, N. Artrith and G. Ceder, Electronic-structure origin of cation disorder in transition-metal oxides, *Phys. Rev. Lett.*, 2017, **119**, 176402.
126 S. Naqash, D. Sebold, F. Tietz and O. Guillon, Microstructure–conductivity relationship of $Na_3Zr_2(SiO_4)_2(PO_4)$ ceramics, *J. Am. Ceram. Soc.*, 2019, **102**, 1057–1070.
127 E. M. Vogel, R. J. Cava and E. Rietman, Na^+ ion conductivity and crystallographic cell characterization in the Hf-NASICON system $Na_{1+x}Hf_2Si_xP_{3-x}O_{12}$, *Solid State Ionics*, 1984, **14**, 1–6.
128 Q. Sun, L. Dai, Y. Tang, J. Sun, W. Meng, T. Luo, L. Wang and S. Liu, Designing a novel electrolyte $Na_{3.2}Hf_2Si_{2.2}P_{0.8}O_{11.85}F_{0.3}$ for all-solid-state Na-O_2 batteries, *Small Methods*, 2022, **6**, 2200345.
129 H. Aono and E. Suginoto, Ionic conductivity and sinterability of NASICON-type ceramics: The systems $NaM_2(PO_4)_3$+$y$$Na_2O$ (M=Ge, Ti, Hf, and Zr), *J. Am. Ceram. Soc.*, 1996, **79**, 2786–2788.
130 P. Yadav and M. C. Bhatnagar, Preparation, structure and conductivity of Sn modified NASICON material, *J. Electroceram.*, 2013, **30**, 145–151.
131 N. S. Bell, C. Edney, J. S. Wheeler, D. Ingersoll and E. D. Spoerke, The influences of excess sodium on low-temperature NASICON synthesis, *J. Am. Ceram. Soc.*, 2014, **97**, 3744–3748.
132 H. Wang, G. Zhao, S. Wang, D. Liu, Z. Mei, Q. An, J. Jiang and H. Guo, Enhanced ionic conductivity of a $Na_3Zr_2Si_2PO_{12}$ solid electrolyte with Na_2SiO_3 obtained by liquid phase sintering for solid-state Na^+ batteries, *Nanoscale*, 2022, **14**, 823–832.
133 Y. B. Rao, K. R. Achary, K. K. Bharathi and L. N. Patro, Enhanced ionic conductivity of Na-excess $Na_3Zr_2Si_2PO_{12}$ solid electrolyte by tuning its elemental composition and sintering temperature, *J. Mater. Sci.*, 2023, **58**, 1–12.
134 S. He, Y. Xu, X. Ma, Y. Chen, J. Lin and C. Wang, Mg^{2+}/F^- synergy to enhance the ionic conductivity of $Na_3Zr_2Si_2PO_{12}$ solid electrolyte for solid-state sodium batteries, *ChemElectroChem*, 2020, **7**, 2087–2094.
135 T. Takahashi, K. Kuwabara and M. Shibata, Solid-state ionics-conductivities of Na^+ ion conductors based on NASICON, *Solid State Ionics*, 1980, **1**, 163–175.
136 M. Samiee, B. Radhakrishnan, Z. Rice, Z. Deng, Y. S. Meng, S. P. Ong and J. Luo, Divalent-doped $Na_3Zr_2Si_2PO_{12}$ natrium superionic conductor: Improving the ionic conductivity *via* simultaneously optimizing the phase and chemistry of the primary and secondary phases, *J. Power Sources*, 2017, **347**, 229–237.
137 L. Shen, J. Yang, G. Liu, M. Avdeev and X. Yao, High ionic conductivity and dendrite-resistant NASICON solid electrolyte for all-solid-state sodium batteries, *Mater. Today Energy*, 2021, **20**, 100691.
138 J. Yang, H.-L. Wan, Z.-H. Zhang, G.-Z. Liu, X.-X. Xu, Y.-S. Hu and X.-Y. Yao, NASICON-structured

$Na_{3.1}Zr_{1.95}Mg_{0.05}Si_2PO_{12}$ solid electrolyte for solid-state sodium batteries, *Rare Met.*, 2018, **37**, 480–487.

139 A. G. Jolley, G. Cohn, G. T. Hitz and E. D. Wachsman, Improving the ionic conductivity of NASICON through aliovalent cation substitution of $Na_3Zr_2Si_2PO_{12}$, *Ionics*, 2015, **21**, 3031–3038.

140 D. Chen, F. Luo, W. Zhou and D. Zhu, Influence of Nb^{5+}, Ti^{4+}, Y^{3+} and Zn^{2+} doped $Na_3Zr_2Si_2PO_{12}$ solid electrolyte on its conductivity, *J. Alloys Compd.*, 2018, **757**, 348–355.

141 H. Tian, S. Liu, L. Deng, L. Wang and L. Dai, New-type Hf-based NASICON electrolyte for solid-state Na-ion batteries with superior long-cycling stability and rate capability, *Energy Storage Mater.*, 2021, **39**, 232–238.

142 E. R. Losilla, M. A. G. Aranda, S. Bruque, J. Sanz, M. A. París, J. Campo and A. R. West, Sodium mobility in the NASICON series $Na_{1+x}Zr_{2-x}In_x(PO_4)_3$, *Chem. Mater.*, 2000, **12**, 2134–2142.

143 Y. Saito, K. Ado, T. Asai, H. Kageyama and O. Nakamura, Ionic conductivity of NASICON-type conductors $Na_{1.5}M_{0.5}Zr_{1.5}(PO_4)_3$ (M: Al^{3+}, Ga^{3+}, Cr^{3+}, Sc^{3+}, Fe^{3+}, In^{3+}, Yb^{3+}, Y^{3+}), *Solid State Ionics*, 1992, **58**, 327–331.

144 S. K. Pal, R. Saha, G. V. Kumar and S. Omar, Designing high ionic conducting NASICON-type $Na_3Zr_2Si_2PO_{12}$ solid-electrolytes for Na-ion batteries, *J. Phys. Chem. C*, 2020, **124**, 9161–9169.

145 S. Lunghammer, D. Prutsch, S. Breuer, D. Rettenwander, I. Hanzu, Q. Ma, F. Tietz and H. M. Wilkening, Fast Na ion transport triggered by rapid ion exchange on local length scales, *Sci. Rep.*, 2018, **8**, 1–8.

146 Y. Deng, C. Eames, L. H. B. Nguyen, O. Pecher, K. J. Griffith, M. Courty, B. Fleutot, J.-N. Chotard, C. P. Grey and M. S. Islam, Crystal structures, local atomic environments, and ion diffusion mechanisms of scandium-substituted sodium superionic conductor (NASICON) solid electrolytes, *Chem. Mater.*, 2018, **30**, 2618–2630.

147 B. Santhoshkumar, P. L. Rao, K. V. Ramanathan, A. K. Bera, S. M. Yusuf, V. R. Hathwar and B. Pahari, Structure and ionic conductivity of $Na_{3+x}Sc_2Si_xP_{3-x}O_{12}$ (x = 0.0, 0.2, 0.4, 0.8) NASICON materials: A combined neutron diffraction, MAS NMR and impedance study, *Solid State Sci.*, 2021, **111**, 106470.

148 Q. Zhang, F. Liang, T. Qu, Y. Yao, W. Ma, B. Yang and Y. Dai, Effect on ionic conductivity of $Na_{3+x}Zr_{2-x}M_xSi_2PO_{12}$ (M = Y, La) by doping rare-earth elements, *IOP Conf. Ser.: Mater. Sci. Eng.*, 2018, **423**, 12122.

149 X. Wang, J. Chen, Z. Mao and D. Wang, Effective resistance to dendrite growth of NASICON solid electrolyte with lower electronic conductivity, *Chem. Eng. J.*, 2022, **427**, 130899.

150 Y. Liu, L. Liu, J. Peng, X. Zhou, D. Liang, L. Zhao, J. Su, B. Zhang, S. Li and N. Zhang, A niobium-substituted sodium superionic conductor with conductivity higher than 5.5 mS cm^{-1} prepared by solution-assisted solid-state reaction method, *J. Power Sources*, 2022, **518**, 230765.